Remote Sensing of Environment 324 (2025) 114738

Contents lists available at ScienceDirect

Remote Sensing of Environment

journal homepage: www.elsevier.com/locate/rse

A gradient-based nonlinear multi-pixel physical method for simultaneously separating component temperature and emissivity from nonisothermal mixed pixels with DART

Zhijun Zhen [a,b], Shengbo Chen [a,c,*], Nicolas Lauret [b], Abdelaziz Kallel [d], Tiangang Yin [e], Jonathan León-Tavares [f], Biao Cao [g], Jean-Philippe Gastellu-Etchegorry [b,**]

[a] The College of Geoexploration Science and Technology, Jilin University, Changchun 130026, China
[b] CESBIO, Université de Toulouse, UT3-Paul Sabatier/CNES/CNRS/INRAE/IRD, 18, Avenue Edouard Belin, 31401 Toulouse, France
[c] Jilin Institute of GF Remote Sensing Application, Changchun 130012, China
[d] Digital Research Center of Sfax, Technopole of Sfax, Sakiet Ezzit 3021, Tunisia
[e] Department of Land Surveying and Geo-Informatics, The Hong Kong Polytechnic University, Hung Hom, Hong Kong
[f] Vlaamse Instelling voor Technologisch Onderzoek (VITO), Boeretang 200, 2400 Mol, Belgium
[g] Innovation Research Center of Satellite Application, Faculty of Geographical Science, Beijing Normal University, Beijing 100875, China

ARTICLE INFO

Edited by Jing M. Chen

Keywords:
Component temperature and emissivity separation
Thermal unmixing
Differentiable radiative transfer
Urban environmental monitoring
Land surface emissivity (LSE)
Land surface temperature (LST)

ABSTRACT

Component temperature and emissivity are crucial for understanding plant physiology and urban thermal dynamics. However, existing thermal infrared unmixing methods face challenges in simultaneous retrieval and multi-component analysis. We propose Thermal Remote sensing Unmixing for Subpixel Temperature and emissivity with the Discrete Anisotropic Radiative Transfer model (TRUST-DART), a gradient-based multi-pixel physical method that simultaneously separates component temperature and emissivity from non-isothermal mixed pixels over urban areas. TRUST-DART utilizes the DART model and requires inputs including at-surface radiance imagery, downwelling sky irradiance, a 3D mock-up with component classification, and standard DART parameters (*e.g.*, spatial resolution and skylight ratio). This method produces maps of component emissivity and temperature. The accuracy of TRUST-DART is evaluated using both vegetation and urban scenes, employing Advanced Spaceborne Thermal Emission and Reflection Radiometer (ASTER) images and DART-simulated pseudo-ASTER images. Results show a residual radiance error is approximately 0.05 W/(m^2·sr). In absence of the co-registration and sensor noise errors, the median residual error of emissivity is approximately 0.02, and the median residual error of temperature is within 1 K. This novel approach significantly advances our ability to analyze thermal properties of urban areas, offering potential breakthroughs in urban environmental monitoring and planning. The source code of TRUST-DART is distributed together with DART (https://dart.omp.eu).

1. Introduction

In the field of thermal remote sensing, component emissivity and temperature are crucial, particularly in studies of vegetation and urban areas (Chen et al., 2011; Jiang et al., 2022; Song et al., 2020). They provide valuable insights into plant physiological processes, including health (Su et al., 2023), productivity (Gonsamo et al., 2015), phenology (Liu et al., 2016), and environmental response (Chen et al., 2016; Zhou et al., 2022). They are major inputs for evapotranspiration models (Chen and Liu, 2020) such as the two-layer, patchwork, and two-source models (Kustas and Norman, 1999; Sánchez et al., 2008). In urban studies, they are essential for understanding the thermal behavior of urban environments (Bian et al., 2024; Chen and Liu, 2020). Monitoring their variations is crucial for energy consumption studies, urban planning (Ru et al., 2023), and mitigating the urban heat island (UHI) (Huang et al., 2017).

The separation of land surface emissivity (LSE) and land surface temperature (LST) from pixels is a complex problem addressed by various methods, categorized as either stepwise or simultaneous (Li et al., 2013; Ru et al., 2023). Stepwise methods, such as single-channel

* Corresponding author at: The College of Geoexploration Science and Technology, Jilin University, Changchun 130026, China.
** Corresponding author.
E-mail addresses: chensb@jlu.edu.cn (S. Chen), jean-philippe.gastellu@iut-tlse3.fr (J.-P. Gastellu-Etchegorry).

https://doi.org/10.1016/j.rse.2025.114738
Received 21 September 2024; Received in revised form 28 March 2025; Accepted 31 March 2025
Available online 17 April 2025

(Ottlé and Vidal-Madjar, 1992), multi-channel (McMillin, 1975; Zheng et al., 2019), and multi-angle methods (Sobrino and Romaguera, 2004), determine LSE first and then retrieve LST using the determined LSE. These methods can introduce significant errors in the retrieved LST when the error in LSE is substantial. Simultaneous methods, such as the gray body method (Barducci and Pippi, 1996), the temperature and emissivity separation (TES) method (Gillespie et al., 1998), the two-temperature method (TTM) (Watson, 1992), and the physics-based day/night operational method (Wan and Li, 1997), retrieve both temperature and emissivity simultaneously (Liu et al., 2022; Wan and Li, 1997). These methods generally yield higher temperature and emissivity retrieval accuracy than stepwise methods.

However, the accuracy of these temperature and emissivity data considerably decreases in heterogeneous scenes (Hu et al., 2022). Indeed, the methods assume pure, isothermal, and flat pixels, which is challenging in Thermal Infrared (TIR) images of urban areas due to their coarse spatial resolutions (Zhen et al., 2022) and high heterogeneity (Ru et al., 2023). For example, Advanced Spaceborne Thermal Emission and Reflection Radiometer (ASTER) LSE products often exhibit step discontinuities (Gustafson et al., 2006; Pivovarník et al., 2016). Unmixing component temperature and emissivity maps from satellite radiance images is a valuable yet challenging task due to factors such as ambiguous definitions of pixel and component emissivity (Cao et al., 2019; Norman and Becker, 1995), temperature within mixed pixels (Roupioz et al., 2023), emissivity directionality (Li et al., 2000), and uncertainties due to the unmixing process (Li et al., 1999; Li et al., 2001).

Various methodologies have been proposed to unmix component temperatures of soil-vegetation mixed pixels. Depending on their mathematical bases, they are classified as either empirical or physical unmixing models (Liu et al., 2020). Alternatively, depending on their data sources, they are categorized into single-source and multi-source models (Liu et al., 2025). Early investigations predominantly utilize single-source empirical/semi-empirical models, whereas more recent studies have increasingly adopted multi-source physical approaches (Liu et al., 2025; Liu et al., 2020).

A typical single-source empirical/semi-empirical model employs Bayesian inversion combined with spatial dependency analysis to extract temperature information from single-band thermal infrared imagery (Zhan et al., 2010). Multi-source empirical/semi-empirical models often integrate the normalized difference vegetation index with brightness factors (Liu et al., 2012) or combine spatial (Markov random field) and temporal (Markov random chain) dependencies to unmix temperature (Kallel et al., 2012). However, these empirical/semi-empirical assumptions can obscure the inherent heterogeneity of land surfaces (Liu et al., 2020).

Table 1
Mathematical variables and corresponding meanings.

Abbreviation	Full name
c	The speed of light
h	Planck constant
k	Boltzmann constant
i	Component
I	Total number of components
λ	Wavelength
Λ	Total number of bands
ε	Pixel emissivity
ε_i	Emissivity of component i
T	Pixel temperature
T_i	Temperature of component i
L_λ	At-surface radiances
E_λ	Downwelling sky irradiance
j	Iteration
J	Total number of iterations
B_λ	Planck's function
S_i	Fraction of component i in a mixed pixel
$G^j_{T,i,\lambda}$	Temperature gradient of component i
$G^j_{\varepsilon,i,\lambda}$	Emissivity gradient of component i

Common single-source physical models comprise multi-angle (Bian et al., 2016; Li et al., 2001), multi-channel (Xie et al., 2016), multi-pixel (Song et al., 2015), and multi-temporal methods (Zhao et al., 2014). The literature (Zhan et al., 2013) details the advantages and limitations of each approach. While these models effectively exploit the unique strengths of their respective data types and are relatively simple to implement, their reliance on a single data source can constrain their ability to capture the full complexity of surface temperature variations. Moreover, they depend on inherent limitations of satellite data, such as cloud interference (Liu et al., 2025). Common multi-source physical models integrate temporal and spatial information or utilize multi-angle and multi-pixel techniques (Bian et al., 2020; Liu et al., 2020) for thermal unmixing. The temporal and spatial approach combines temporal and spatial data using a diurnal temperature cycle model paired with a spatial sliding window (Liu et al., 2020). The multi-angle and multi-pixel method employs dual-angle observations alongside multi-pixel information to reduce spatial mismatches (Bian et al., 2020). Multi-source physical models enhance both accuracy and practicality, mitigating some limitations inherent to single-type methods. However, due to the reliance on satellite data, trade-offs between spatial and temporal resolution remain, and challenges such as cloud cover and other remote sensing limitations cannot be entirely overcome (Liu et al., 2025).

The state-of-the-art methodology relies on multi-source data fusion principles (Ding et al., 2023), which synergistically integrates the inherent strengths of empirical/semi-empirical frameworks with physical models to establish sophisticated multi-source hybrid models. The multi-source data fusion-based global surface soil and vegetation temperature retrieval method (FuSVeT) (Liu et al., 2025) is a representative example. It includes methodological innovation by incorporating physically-based models, such as the diurnal temperature cycle model, to characterize temporal temperature fluctuations and systematically reduce parameterization uncertainties. It uses diverse empirical data streams, including MOderate Resolution Imaging Spectroradiometer (MODIS) satellite observations and European Centre for Medium-range Weather Forecasts reanalysis 5th generation (ERA5)-Land datasets. This greatly improves the spatial coverage and temporal resolution of results. However, these methods often only consider soil and vegetation, limiting their applications in multi-component analysis.

Several unmixing methods have been proposed to separate component temperature and emissivity in urban areas characterized by the presence of multiple constituents (Cubero-Castan et al., 2014; Granero-Belinchon et al., 2020). For example, the Thermal Remote Sensing Unmixing for Subpixel Temperature (TRUST) method estimates intra-pixel abundances and component temperatures in straightforward scenarios, such as three-material roofs (Cubero-Castan et al., 2014). Its multitemporal variant, TRUST Day and Night Synergy (TRUST-DNS), reduces the algorithm's requirements for spatial and spectral resolution by using day and night image pairs (Granero-Belinchon et al., 2020). However, their linear unmixing models inadequately address the multiple scattering phenomena resulting from heterogeneous land cover interactions. Additionally, they struggle to simultaneously separate temperature and emissivity due to the assumption of spatially constant component emissivity. Simultaneously retrieving component temperature and emissivity is crucial (Mitraka et al., 2012) as an error on emissivity of 0.01 leads to an error on the LST of around 0.6 K (Jiménez-Muñoz and Sobrino, 2003). A recent study (Chen et al., 2021) used nonlinear unmixing techniques that consider geometric effects by using the sky view factor (*i.e.*, a ratio of radiation received by a planar surface from the sky to that received from the entire hemispheric radiating environment). However, this method provides urban flat surface temperature and emissivity, not an unmixing.

3D radiative transfer models, together with the growing availability of 3D urban mock-up, offer a great potential for TIR unmixing. Note that abundance can be inaccurate as highly emitting objects, even small, can greatly dominate the radiance of a mixed pixel (Bioucas-Dias et al.,

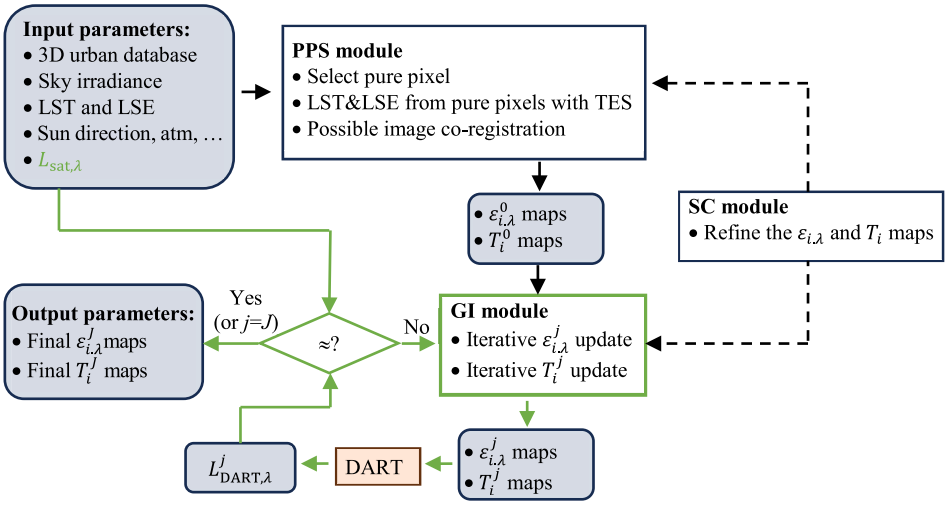

Fig. 1. Algorithm flow chart: input, intermediate, and output parameters (rounded rectangles), processes (square corner rectangles), decision (rhombus). j: current iteration. J: maximum iteration. $L_{sat,\lambda}$: satellite at-surface radiance image. $L^j_{DART,\lambda}$: DART simulated radiance image at wavelength λ at iteration j. $\varepsilon^j_{i,\lambda}$: emissivity of component i at wavelength λ at iteration j. T^j_i: temperature of component i at iteration j. PPS: pure pixel selection. GI: gradient iteration. SC: spectral correlation. LST: land surface temperature. LSE: land surface emissivity.

2012). The 3D urban mock-up can identify the types of endmembers in a pixel, and the spectral gradient calculated by 3D radiative transfer can replace the abundance to represent the radiance contribution percentage. For instance, based on the nonlinear unmixing method, the Discrete Anisotropic Radiative Transfer (DART) calibration method (Landier et al., 2018) and Unmixing Spectral (US)-DART (Zhen et al., 2025) successfully retrieve component optical properties of urban and vegetation areas (Zhen et al., 2021). However, they cannot retrieve component emissivity and temperature in the long waves.

Here, we propose a comprehensive physically-based multi-source multi-pixel TIR nonlinear unmixing method that combines remote sensing physics, geostatistics, computer graphics, and gradient-based learning: the Thermal Remote sensing Unmixing for Subpixel Temperature and emissivity with DART (TRUST-DART). Compared to existing TIR unmixing models, it allows a simultaneous retrieval of component temperature and emissivity, and applications in multi-component analysis (*i.e.*, more than soil and vegetation components). Its accuracy is evaluated using two types of scenes (vegetation and urban) and images (ASTER images and pseudo-ASTER images simulated by DART). Table 1 presents the mathematical variables and their definitions used here. The contributions of this work are summarized as follows:

- A novel method named TRUST-DART simultaneously separates the component temperature and emissivity of non-isothermal mixed pixels.
- TRUST-DART unmix urban scenes that contain multi-components rather than only soil-vegetation mixed scenes.
- TRUST-DART is a gradient-based nonlinear physically unmixing method that propagates gradients among physical parameters.

2. Methodology and data

Section 2.1 presents necessary knowledge of the DART model. Section 2.2 presents the theoretical framework and associated formulas of the TRUST-DART. Section 2.3 presents the experimental data for accuracy assessments.

2.1. DART model

DART (Gastellu-Etchegorry, 2008; Gastellu-Etchegorry et al., 2017; Gastellu-Etchegorry et al., 2015; Gastellu-Etchegorry et al., 2016) is a robust physics-based 3D Earth-atmosphere radiative transfer model, from the visible to thermal infrared domains. It simulates remote sensing images of urban and natural landscapes with topography accurately and efficiently. Landscapes are 3D arrays of facets (triangles), fluids (*e.g.*, atmosphere/smoke), and turbid volumes (*e.g.*, vegetation). Turbid volumes have infinitely small facets with Lambertian/non-Lambertian optical properties. DART can import complex landscapes (*e.g.*, forest/urban 3D mock-up) for detailed geometry, including vegetation and water bodies. Developed at the Centre for Space Studies of the Biosphere (CESBIO) since 1992 and patented in 2003, DART is available for non-commercial academic and research use (https://dart.omp.eu).

DART serves as a vital tool for exploring mixing and unmixing processes. Since 2018, DART involves a so-called Lux mode that incorporates a Monte Carlo differentiable radiative transfer framework (Wang et al., 2024b), which improves simulation efficiency and allows the calculation of radiance gradients. Here, DART was used to generate pseudo-ASTER images (*i.e.*, L_λ and E_λ), providing test data for evaluating the accuracy of TRUST-DART. DART was also used to calculate both the component fraction and the gradient for unmixing.

2.2. Thermal remote sensing unmixing for subpixel temperature and emissivity: TRUST-DART

TRUST-DART is an iterative optimization algorithm that simultaneously separates component temperature and emissivity over non-isothermal mixed pixels using multispectral TIR images. It necessitates several input parameters, including a tagged (used to determine the number of components per pixel) 3D urban mock-up, a satellite at-surface radiance image $L_{sat,\lambda}$, downwelling sky irradiance E_λ, and other common DART input parameters (*e.g.*, spatial resolution and skylight ratio). Its optional parameters include LSE and LST maps. If these optional inputs are unavailable, the algorithm retrieves LSE and LST using the TES method from $L_{sat,\lambda}$ and E_λ. Its outputs include the component emissivity $\varepsilon_{i,\lambda}$ and temperature T_i maps.

TRUST-DART consists of a core gradient iteration (GI) module that uses two auxiliary modules: pure pixel selection (PPS) and spectral correlation (SC) (Fig. 1). The PPS module determines the initial emissivity ($\varepsilon^{PPS}_{i,\lambda}$) and temperature ($T^{PPS}_i$) of each component. These initial values are refined by the GI module, which iteratively optimizes component emissivity ($\varepsilon^{GI}_{i,\lambda}$) and temperature ($T^{GI}_i$). The SC module is run

at the end of each module or each iteration of GI to correct erroneous pixels using pre-defined SC rules.

The GI module refines the initial values ($\varepsilon_{i,\lambda}^{\mathrm{PPS}}$ and T_i^{PPS}) through an iterative approach using temperature and emissivity gradients. These gradients are determined by differentiating the temperature and emissivity terms of the radiative transfer equation. For a flat mixed pixel with I components, the at-surface radiances (L_λ) is

$$L_\lambda = \sum_i^I S_i \cdot \left[\varepsilon_{i,\lambda} B_\lambda(T_i) + (1-\varepsilon_{i,\lambda}) \frac{E_\lambda}{\pi} \right] \quad (1)$$

where i is component, λ is wavelength, E_λ is the downwelling sky irradiance, $\varepsilon_{i,\lambda}$ is component emissivity, T_i is component temperature, S_i is component fraction, $B_\lambda(T_i)$ is Planck's function, which is

$$B_\lambda(T_i) = \frac{2c^2 h}{\lambda^5 \left(e^{\frac{h \cdot c}{\lambda \cdot k \cdot T_i}} - 1 \right)} \quad (2)$$

with Planck constant $h \approx 6.63 \times 10^{-34}$ J·s, Boltzmann constant $k \approx 1.3807 \times 10^{-23}$ J·K^{-1}, the speed of light $c \approx 2.9979 \times 10^{8}$ m·s^{-1}.

The gradient $G_{T,i,\lambda}^j$ of radiance relative to temperature is

$$G_{T,i,\lambda}^j = \frac{\partial L_\lambda^j}{\partial T_i} = \frac{2 S_i c^3 \varepsilon_{i,\lambda}^j h^2 e^{\frac{ch}{kT_i^j \lambda}}}{k \left(T_i^j\right)^2 \lambda^6 e^{\frac{2ch}{kT_i^j \lambda}} - 2k \left(T_i^j\right)^2 \lambda^6 e^{\frac{ch}{kT_i^j \lambda}} + k \left(T_i^j\right)^2 \lambda^6} \quad (3)$$

where j is iteration in the GI module. Similarly, the gradient $G_{\varepsilon,i,\lambda}^j$ of radiance relative to the emissivity is

$$G_{\varepsilon,i,\lambda}^j = \frac{\partial L_\lambda^j}{\partial \varepsilon_{i,\lambda}} = S_i \left[\frac{2c^2 h}{\lambda^5 \left(e^{\frac{ch}{kT_i^j \lambda}} - 1 \right)} - \frac{E_\lambda}{\pi} \right] \quad (4)$$

DART can simulate $G_{T,i,\lambda}^j$ and $G_{T,i,\lambda}^j$ simultaneously in addition to the images of the considered 3D landscape. In the inversion algorithm, the DART-simulated radiance at iteration $j+1$ is assessed as the sum of the current radiance with gradient-based adjustments. The differential 3D radiative transfer equation for thermal infrared is:

$$L_{\mathrm{DART},\lambda}^{j+1} = L_{\mathrm{DART},\lambda}^j + \sum_{i=1}^I \left[G_{\varepsilon,i,\lambda}^j \cdot \left(\varepsilon_{i,\lambda}^{j+1} - \varepsilon_{i,\lambda}^j \right) \right] + \sum_{i=1}^I \left[G_{T,i,\lambda}^j \cdot \left(T_i^{j+1} - T_i^j \right) \right] \quad (5)$$

where $L_{\mathrm{DART},\lambda}^j$ is the DART simulated radiance image at iteration j, $G_{\varepsilon,i,\lambda}^j$ and $G_{T,i,\lambda}^j$ are the emissivity and temperature gradients calculated by DART with $\varepsilon_{i,\lambda}^j$ and T_i^j, $\varepsilon_{i,\lambda}^{j+1}$ and $\varepsilon_{i,\lambda}^j$ are the emissivity, and T_i^{j+1} and T_i^j are the temperatures at two consecutive iterations, j and $j+1$.

Iteration continues until the simulated radiance converges to the satellite image radiance. Therefore, Eq. (5) is rewritten as:

$$L_{\mathrm{sat},\lambda} = L_{\mathrm{DART},\lambda}^j + \sum_{i=1}^I \left[G_{\varepsilon,i,\lambda}^j \cdot \left(\varepsilon_{i,\lambda}^{j+1} - \varepsilon_{i,\lambda}^j \right) \right] + \sum_{i=1}^I \left[G_{T,i,\lambda}^j \cdot \left(T_i^{j+1} - T_i^j \right) \right] \quad (6)$$

In Eq. (6), $L_{\mathrm{sat},\lambda}$ is from the satellite image, $\varepsilon_{i,\lambda}^j$ and T_i^j are DART input parameters at the previous iteration (known parameter). For the first iteration ($j=1$), the initial values are from the PPS module that determines pure pixels. $L_{\mathrm{DART},\lambda}^j$, $G_{\varepsilon,i,\lambda}^j$, $G_{T,i,\lambda}^j$ are calculated by DART using radiative transfer. $\varepsilon_{i,\lambda}^{j+1}$ and T_i^{j+1} are the unknowns. DART uses them at the next iteration. Therefore, each iteration uses the value from the j iteration to determine the unknown parameters at $j+1$. This iterative process stops if the difference between $L_{\mathrm{DART},\lambda}^j$ and $L_{\mathrm{sat},\lambda}$ falls below a user-specified threshold or if the iteration number reaches a user-specified maximum value.

To address the underdetermined nature of the TIR equation system, a multi-pixel approach is used: identical components in adjacent pixels are assumed to have equal emissivity and temperature values. This approach increases the number of equations, ensuring a solvable system. For one pixel, the number of equations of Eq. (6) is the number of bands Λ (*e.g.*, $\Lambda = 5$ for ASTER). The number of unknowns depends on Λ and the number of elements I. It is $\Lambda \times I$ (emissivity) $+ I$ (temperature), which is much smaller than the number of equations, leading to possible underdetermination (*i.e.*, an infinite number of solutions). The multi-pixel method is used to increase the number of equations, by assuming that the same components i in adjacent pixels share identical T_i^{j+1} and $\varepsilon_{i,\lambda}^{j+1}$ per band. Thus, if an analysis window has M pixels, the total number of equations in the system is $M \times \Lambda$. The full equation system is:

$$\begin{bmatrix} L_{\mathrm{sat},\lambda}(1) \\ \cdots \\ L_{\mathrm{sat},\Lambda}(1) \\ \cdots \\ L_{\mathrm{sat},\Lambda}(M) \end{bmatrix} = \begin{bmatrix} L_{\mathrm{DART},\lambda}^j(1) \\ \cdots \\ L_{\mathrm{DART},\Lambda}^j(1) \\ \cdots \\ L_{\mathrm{DART},\Lambda}^j(M) \end{bmatrix} - \begin{bmatrix} \sum_{i=1}^I \left[G_{\varepsilon,i,\lambda}^j(1) \cdot \varepsilon_{i,\lambda}^j(1) + G_{T,i,\lambda}^j(1) \cdot T_i^j(1) \right] \\ \cdots \\ \sum_{i=1}^I \left[G_{\varepsilon,i,\Lambda}^j(1) . \varepsilon_{i,\Lambda}^j(1) + G_{T,i,\Lambda}^j(1) . T_i^j(1) \right] \\ \cdots \\ \sum_{i=1}^I \left[G_{\varepsilon,i,\Lambda}^j(M) . \varepsilon_{i,\Lambda}^j(M) + G_{T,i,\Lambda}^j(M) . T_i^j(M) \right] \end{bmatrix} + \begin{bmatrix} G_{T,1,\lambda}^j(1) & \ldots & G_{T,I,\lambda}^j(1) & G_{\varepsilon,1,\lambda}^j(1) & \ldots & G_{\varepsilon,I,\lambda}^j(1) \\ \ldots & \ldots & \ldots & \ldots & \ldots & \ldots \\ G_{T,1,\Lambda}^j(1) & \ldots & G_{T,I,\Lambda}^j(1) & G_{\varepsilon,1,\Lambda}^j(1) & \ldots & G_{\varepsilon,I,\Lambda}^j(1) \\ \ldots & \ldots & \ldots & \ldots & \ldots & \ldots \\ G_{T,1,\Lambda}^j(M) & \ldots & G_{T,I,\Lambda}^j(M) & G_{\varepsilon,1,\Lambda}^j(M) & \ldots & G_{\varepsilon,I,\Lambda}^j(M) \end{bmatrix} \cdot \begin{bmatrix} T_1^{j+1}(\beta) \\ \ldots \\ T_I^{j+1}(\beta) \\ \varepsilon_{1,\alpha}^{j+1}(\beta) \\ \ldots \\ \varepsilon_{I,\alpha}^{j+1}(\beta) \end{bmatrix} \quad (7)$$

where $\alpha \in \{\lambda, \Lambda\}$ and $\beta \in \{1, M\}$. To solve this equation system, $M \times \Lambda$ must be larger than $(\Lambda + 1) \times I$. Therefore, the size and shape of each window can be customized based on the number of components and spatial distribution pattern to get a well-conditioned equation system. The window size is determined using several factors. First, the window must satisfy the underlying assumption that component temperatures are equal within it. Second, the size must accommodate the number of components present in the mock-up. From a mathematical perspective, the window size M must be sufficiently large to encompass enough pixels for solving the equation system. However, from a physical standpoint, M should remain small enough to maintain the validity of uniform component temperature and emissivity within the window. Given that both the satellite's spatial resolution and the distribution of components within pixels are fixed, our approach prioritizes smaller windows to meet the physical assumption. For more complex cases where pixels contain many components, the algorithm progressively expands the window size to ensure solution feasibility. Not all pixels are solvable at one window shape, and unresolved pixels are revisited when the next processing window passes through, and a median filter is applied to fill gaps in the emissivity and temperature maps.

When solving the equation system, the results $\varepsilon_{i,\lambda}^{PPS}$ and T_i^{PPS} of the PPS module (or previous iteration results $\varepsilon_{i,\lambda}^{j}$ and T_i^{j} of the GI module) are used as the initial values, and constraint conditions are applied to limit the boundary of the solved $\varepsilon_{i,\lambda}^{j}$ and T_i^{j} to restrain the generated noises and keep good spatial coherence. Boundary constraints are commonly used in equation system solving to separate the component temperature of vegetation and soil (Liu et al., 2020). Here these conditions are set as (1 ± threshold of emissivity) × $\varepsilon_{i,\lambda}^{j}$ and (1 ± threshold of temperature) × T_i^{j}. In the case of remote sensing images without any noise (*i.e.*, DART simulated remote sensing images), the boundary constraints can be set very wide or even without the boundary. For the ASTER image, inaccuracies (*e.g.*, arising from co-registration, atmosphere, and city modeling) cause errors in calculating emissivity and temperature gradients, necessitating a boundary to reduce noise. Typically, narrower boundaries are needed if these inaccuracies are high. In our experiment, thresholds of 1.5 % for emissivity and 0.5 % for temperature yield better results.

The PPS module identifies pure pixels to provide the initial values of emissivity $\varepsilon_{i,\lambda}^{PPS}$ and temperature T_i^{PPS} from LSE and LST maps for the GI module. If not available, the LSE and LST maps are estimated using the TES method (Gillespie et al., 1998). The DART model calculates the S_i per pixel using the city mock-up and typical properties from DART database, and pure pixels are selected using a threshold, initially set at 0.9 and gradually reduced to 0.1 in increments of 0.1 if necessary. This process can provide many pure pixels, for example in very high spatial resolution images. Then, to mitigate co-registration discrepancies between the city mock-up and the satellite image, an erosion process can eliminate the boundaries of the zones of pure pixels. If no pure pixels are identified, the user selects emissivity and temperature values from the DART database. If pixels are identified as pure, their LST and LSE are assigned to the mixed pixels of the corresponding component type. The values of $\varepsilon_{i,\lambda}^{PPS}$ and T_i^{PPS} of mixed pixels are set to those of their nearest (in terms of Euclidean distance) pure pixel, ensuring spatial continuity. For that, a growing neighborhood is used. If the neighborhood of a mixed pixel contains several pure pixels, the median value of these pure pixels is used. The PPS module is crucial for initialization because LST retrieval error significantly affects component temperature separation (Liu et al., 2020). The derived values not only initiate iterative refinement but also inform land cover gradient calculations.

The SC module corrects erroneous pixels in the emissivity and temperature maps by applying user-defined optical and thermal rules. These rules, which function like band operations, support arithmetic operators (+, −, ×, /), relational operators (>, ≥, <, ≤), and logical operators (&, |) with the option to modify precedence using parentheses. Emissivity comparisons are between bands within a component, whereas temperature comparisons are across different components (*e.g.*, water generally has a lower temperature than ground in the day and a higher temperature at night). Pixels that violate these rules are removed and replaced using a median filter. This filter is chosen for its ability to preserve edge features, reduce noise, and provide robust, minimally biased estimates for missing values. Preliminary analysis showed that, given the inherent noise from uncontrolled variables (*e.g.*, 3D mock-up, co-registration errors, and atmosphere effect), the median filter outperforms the mean filter, aligning with previous research (Hyndman and Koehler, 2006; Mitraka et al., 2012) that favors median-based approaches for asymmetric error distributions in landscape studies.

2.3. Data

Section 2.3.1 presents the study areas and their corresponding 3D mock-up. Section 2.3.2 presents the *in situ* measured water body temperature and the distribution of the sampling points. Section 2.3.3 presents the optical and temperature properties assigned per component of the 3D mock-up. Section 2.3.4 presents the optical satellite images and their preprocessing.

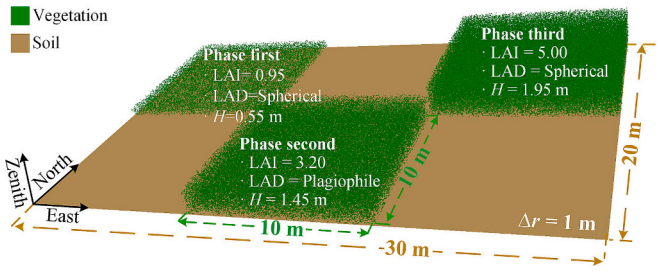

Fig. 2. The 3D mock-up of the maize scene. The scene consists of adjacent vegetation plots and bare ground. The geometric parameters of the canopies refer to the three development phases of the maize canopy. The leaf area index (LAI) is defined for each vegetation plot rather than the entire scene. LAD: leaf angle distribution. *H*: canopy height. Δ*r*: spatial resolution.

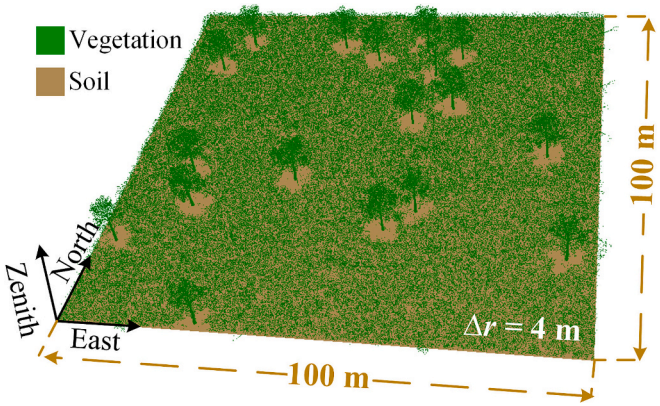

Fig. 3. The 3D mock-up of the arid area distributed trees from RAMI scenario (HET50_SAV_PRE). The scene is created based on Kruger National Park (KNP), South Africa. These plots encompass an arid heterogeneous savanna ecosystem characterized by an overstory tree layer and an understory grass layer.

2.3.1. Scene 3D mock-up

Two kinds of scenes, including vegetation and urban, were used to validate TRUST-DART.

2.3.1.1. Vegetation 3D mock-up. Two vegetation scenes, one maize scene and one sparsely distributed tree scene, were used. The maize scene, spanning 30 m × 20 m with a spatial resolution of 1 m, includes three homogeneous maize canopies and three flat bare ground. Each canopy covers an area of 10 m × 10 m and represents a different developmental phase (Fig. 2). As the phases advance, both the leaf area index (LAI) and the vegetation height increase. The LAI rises from 0.95 to 5.00, while the height increases from 0.55 m to 1.95 m. Two leaf angle distribution (LAD) types, spherical and plagiophile, were used to account for a broad spectrum of scenarios. These parameters were set in line with the literature (Duthoit et al., 2008) to simulate a homogeneous maize canopy at three growth stages using DART. The LAIs are specified per vegetation plot.

The RAMI scenario (RAMI5, 2021) was used to consider a scene with sparsely distributed trees (Fig. 3). It corresponds to the Kruger National Park (KNP), South Africa, within two long-term fire ecology experimental plots at Skukuza (25.1097°S, 31.4172°E) and Pretoriuskop (25.1639°S, 31.2340°E) (Van Wilgen et al., 2004). These plots encompass an arid heterogeneous savanna ecosystem characterized by an overstory tree layer and an understory grass layer. The vegetation at the Skukuza plots is primarily composed of shallow-rooted deciduous Combretum species, including red bushwillow, russet bushwillow, and

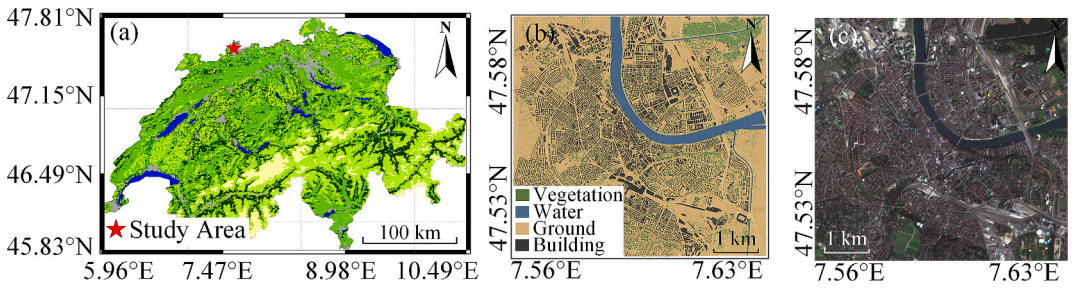

Fig. 4. The study area of Basel. (a) Moderate Resolution Imaging Spectroradiometer (MODIS) land-cover type yearly map in Switzerland. (b) 3D mock-up of Basel. Blue: water; green: vegetation; yellow: ground; black: buildings. (c) The true RGB composites of PlanetScope image of Basel. (For interpretation of the references to colour in this figure legend, the reader is referred to the web version of this article.)

mixed bushwillow. The understory consists predominantly of grasses (Disney et al., 2011).

Detailed *in situ* measurements of tree height, diameter at breast height (DBH), crown size, and LAI were used to get a realistic 3D mock-up of trees and grasses to simulate the 100 × 100 m savanna scene. The tree spatial distribution follows a predefined density distribution derived from field observations. Additionally, standing and fallen tree structures were incorporated to reflect the natural variability observed in the field. The understory grass layer is represented using cylindrical objects of varying lengths to balance computational efficiency with structural realism. Given the extensive grass cover, approximately 200,000 individual grass plants are distributed randomly over the 1 ha plot. These mock-ups were designed to approximate the scattering and transmission characteristics of real grass canopies.

2.3.1.2. Urban 3D mock-up. Two European cities were used, Basel in Switzerland and Brussels in Belgium. Each city has unique topographies influencing urban architecture, and consequently their energy balance.

Situated in the far north of Switzerland, Basel is nestled among hills and mountains in the Rhine Valley (Fig. 4). It is located at 47° 33′ 17″ N, 7° 35′ 26″ E, around 300 m above sea level. It experiences a moderately continental climate, with cold winters and warm summers (Zhen et al., 2022). The average temperature varies from 2.3 °C in January to 20.3 °C in July. The city receives approximately 850 mm of annual precipitation, with May being the wettest month and February the driest. The UHI effect in Basel has an average nocturnal heat island intensity of approximately 2 °C, peaking at 5.3 °C (Wicki et al., 2018). The 3D city mock-up (Landier, 2018; Landier et al., 2018) was initially created with four land-cover types (ground, water, buildings, and vegetation) for assessing the urban anthropogenic heat flux from Earth observation satellites in the URBan ANthrpogenic heat FLUX from Earth observation Satellites (URBANFLUXES) project (Chrysoulakis et al., 2018). The location and geometric structure of all urban components, including the local digital elevation model (DEM), are from local urban databases. Tree location, height, and crown dimensions are from measurements. Here, DART simulates trunks as regular octahedrons and crowns as ellipsoidal volumes filled homogeneously with small triangles to mimic the so-called turbid medium (*i.e.*, an infinite number of infinitely small facets with a statistical angular orientation) commonly used in modeling works for remote sensing studies. However, due to administrative issues, tree and building data at the left bottom corner (around 47° 32′ 25″ N, 7° 34′ 0″ E) are unavailable. The final 3D mock-up covers ~5 km × ~5 km with over 78,000 trees. More detailed information on the urban mock-up is given by (Landier, 2018; Zhen et al., 2021).

Brussels is located on a plateau crisscrossed by numerous rivers and valleys, in the north-central part of Belgium, approximately 180 km from the country's southern tip (Fig. 5). Its geographical coordinates are 50° 51′ 0″ N, 4° 21′ 0″ E, around 15 m above sea level. It has a temperate climate with four distinct seasons. Temperatures are relatively mild year-round, with the average low at 1 °C in winter and peaking at 23 °C in summer. Its mean UHI intensity is 3.22 °C, with heat wave days in the city increasing at double the rate of rural areas (Lauwaet et al., 2016). The 3D geometry of Brussels, sourced from Urbis (https://datastore.brussels/web/urbis-download), was converted to OBJ format and merged into a single file. Defaults in the 3D mock-up (*e.g.*, misclassified roofs and DEM holes) were rectified with Python scripts and Blender software. The mock-up was converted from the national geo-reference system (EPSG:31370) to the international system (EPSG:32631). The final mock-up covers ~16.5 km × ~16.5 km with over 100 million triangles. It was supplemented with tree geometry data from Vrije Universiteit Brussel, detailing over 1.4 million trees. However, due to administrative issues, tree data for three small areas (around 4.366°E, 50.887°N; 4.324°E, 50.865°N; and 4.458°E, 50.848°N) are unavailable.

2.3.2. In situ measured water temperature

Field measured water temperature was obtained from HYDRIA (https://hydria.be/fr/carte-interactive-des-sites/), a public limited company, responsible for the collection and treatment of wastewater from the Senne basin. We carefully checked all the data and found 5 stations (Senne OUT, Senne Elia, Canal Béco, Senne Vétérinaire, Senne Viangros

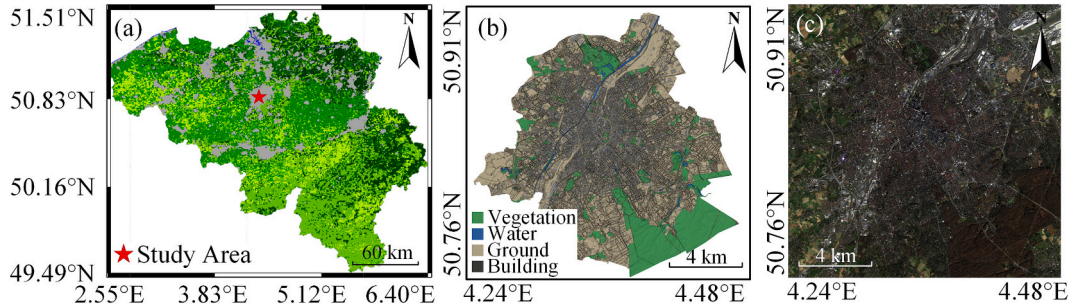

Fig. 5. The study area of Brussels. (a) Moderate Resolution Imaging Spectroradiometer (MODIS) land-cover type yearly map in Belgium. (b) 3D mock-up of Brussels. Blue: water; green: vegetation; yellow: ground; black: buildings. (c) The true RGB composites of PlanetScope image of Brussels. (For interpretation of the references to colour in this figure legend, the reader is referred to the web version of this article.)

Table 2
The coordinates (EPSG: 31370) and measured water temperature of the Brussels' stations. Water body temperature is measured at April 7, 2024 12:18:40 (CEST, UTC + 2).

Site name	X (m)	Y (m)	Temperature (℃)
Senne OUT	153,138.99971	177,763.00027	14.04
Senne Elia	150,758.96478	174,519.101605	13.78
Canal Béco	148,792.62956	172,710.74679	13.32
Senne Vétérinaire	147,265.78987	169,033.91732	14.04
Senne Viangros IN	145,351.38972	167,149.68173	13.77

Table 3
Optical ($\varepsilon_{\lambda,i}$) and temperature (T_i) properties of each component i for the pseudo-ASTER image simulation. $\varepsilon_{\lambda,i}$ are resampled to the spectral response function of the ASTER sensor.

Components	T_i (K)	$\varepsilon_{\lambda,i}$				
		8.3 μm	8.65 μm	9.1 μm	10.6 μm	11.3 μm
Vegetation	305.65	0.9726	0.9656	0.9573	0.9597	0.9628
Buildings	304.90	0.9545	0.9511	0.9455	0.9305	0.9307
Water	302.42	0.9830	0.9838	0.9850	0.9906	0.9904
Ground	311.65	0.9828	0.9822	0.9781	0.9703	0.9669

IN) that measured water body temperature (Table 2). Based on the available dates of the measured data and ASTER transit time, we selected the temperature data at April 7, 2024 12:18:40 Central European Summer Time (CEST), Coordinated Universal Time (UTC) + 2. Then, the ASTER data (ID: 00304072024101840) was input into TRUST-DART, and its outputs were compared with measured water temperature for accuracy assessment.

2.3.3. Optical and temperature properties

To assess the accuracy of TRUST-DART, we simulated with DART a pseudo-ASTER image. We used optical and temperature properties (Table 3) from the ASTER or DART spectral databases (Zhen et al., 2022) that we resampled using the ASTER spectral response function. The hour being the time of day, ground has the highest temperature, followed by vegetation and buildings, followed by water, with a reasonable temperature difference between soil and vegetation (Jiang et al., 2024; Liu et al., 2020). To align with TRUST-DART's assumption that identical components in a sampling window have the same properties, optical and temperature properties are spatially invariant for each component. This avoids complications such as two temperature values per component depending on if it is sunlit or shaded, and simplifies error calculations.

2.3.4. Satellite data and preprocessing

This study employed satellite images from the ASTER and Ecosystem Spaceborne Thermal Radiometer Experiment on the Space Station (ECOSTRESS). ASTER, a multispectral imaging instrument developed jointly by Japan's METI and NASA, was launched aboard NASA's Terra satellite in 1999. It provides high spatial resolution data across VNIR, SWIR, and TIR wavelengths. It has five TIR spectral bands from 8.125 μm to 11.65 μm with a spatial resolution of 90 m. Each image covers a 60 × 60 km^2 area. Its sun-synchronous orbit allows a nominal repeat cycle of 16 days. We used 3 ASTER TIR products: surface radiance (L2), kinetic temperature (L2), and emissivity (L2) (Abrams et al., 2002).

ECOSTRESS is an ongoing International Space Station (ISS) experiment that measures TIR radiance in five spectral bands from 8 to 12 μm at a resolution of 70 m. Each image covers approximately a 400 × 400 km^2 area. Launched in mid-2018, it initially operated in five-band mode, but the 8.285 μm and 9.060 μm bands contain fill values from May 2019 to May 2023; full five-band operations resumed thereafter. Its products include top-of-atmosphere radiance, cloud masks, LST, and LSE products. In contrast to ASTER, ECOSTRESS does not provide surface radiance products directly to the users. Table 4 shows the ASTER and ECOSTRESS central wavelengths, spectral bandwidths, and spatial resolutions.

Table 4
Thermal band spectral information of ASTER and ECOSTRESS. Data are from the USGS website (https://lpdaac.usgs.gov/data/get-started-data/collection-overview/missions/aster-overview/) and ECOSTRESS product specifications (Thomas and William, 2015). λ: central wavelength, $\Delta\lambda$: spectral bandwidth, Δr: spatial resolution.

ASTER				ECOSTRESS			
Bands	λ (μm)	$\Delta\lambda$ (μm)	Δr (m)	Bands	λ (μm)	$\Delta\lambda$ (μm)	Δr (m)
B10	8.300	0.350	90	B1	8.285	0.340	70
B11	8.650	0.350	90	B2	8.785	0.350	70
B12	9.100	0.350	90	B3	9.060	0.360	70
B13	10.600	0.700	90	B4	10.522	0.540	70
B14	11.300	0.700	90	B5	12.001	0.520	70

The ASTER images were treated by TRUST-DART, while ECOSTRESS images were used for auxiliary comparisons. For example, ECOSTRESS LSE was compared with the retrieved component emissivity maps, and ECOSTRESS LST was used to analyze the LST in the Brussels area, to confirm that apparent anomalies were not sensor artifacts. Basel and Brussels ASTER and ECOSTRESS images were meticulously selected to ensure a minimal time gap between them. During this selection process, priority was given to the availability of all five bands of ECOSTRESS and to minimizing the interval between ECOSTRESS and ASTER. This strategy was implemented to ensure that the emissivity of the components did not undergo significant variations over a brief period.

For Basel, the ASTER image (ID: 00309192018211) was acquired on September 19, 2018, at 21:19:43 UTC, while its ECOSTRESS image (ID: 01139_009_20180918T020025_0601) was acquired on September 18, 2018, at 02:00:25 UTC. Their time difference is ≈43.32 h. For Brussels, the ASTER image (ID: 0030926201821264) is from September 26, 2018, at 21:26:43 UTC, while its ECOSTRESS image (ID: 01275_002_20180926T194920_0601) is from the same day at 19:49:20 UTC, which corresponds to a time difference ≈1.62 h (Table 5). Figs. 7 and 8 display the selected ASTER and ECOSTRESS images, respectively.

The preprocessing procedure involved data reprojection and co-registration. To mitigate the impact of resampling on image spectral quality, we reprojected the urban mock-ups to their respective satellite coordinates, specifically World Geodetic System (WGS) 1984 Universal Transverse Mercator (UTM) Zone 32 N for Basel and WGS 1984 UTM Zone 31 N for Brussels. For the co-registration process between the ASTER and DART images, we used the Geoscience Extended Flow Optical Lucas-Kanade Iterative (GeFolki) software (Brigot et al., 2016; Plyer et al., 2015) of the French Aerospace Lab (ONERA) (https://github.com/aplyer/gefolki). This software claims a theoretical geometric accuracy of 0.1 pixels.

3. Application and accuracy assessment of TRUST-DART

We evaluated the accuracy of TRUST-DART using vegetation and urban scenes. Section 3.1 presents two vegetation applications and accuracy assessments. Section 3.2 presents two urban applications and accuracy assessments.

3.1. Application on vegetation scenes

Two pseudo-satellite vegetation images (*i.e.*, maize and forest), simulated by DART, were used to evaluate the accuracy of TRUST-DART on vegetation. Section 3.1.1 presents visual comparisons at the inversion final iteration, and Section 3.1.2 presents the quantitative accuracy at each iteration.

3.1.1. Visual accuracy assessment

Fig. 9 shows RGB false colour composites of the retrieved ground and

Table 5
Parameters of ASTER and ECOSTRESS imagery in Basel and Brussels.

Parameters	Values			
Study areas	Basel		Brussels	
Satellite	ASTER	ECOSTRESS	ASTER	ECOSTRESS
ID	00309192018211943	01139_009_20180918T020025_0601	00309262018212643	01275_002_20180926T194920_0601
Date (UTC)	2018.09.19 21:19:43	2018.09.18 02:00:25	2018.09.26 21:26:43	2018.09.26 19:49:20

Table 6
Temperature statistics of the maize scene. SD: standard deviation. IQR: interquartile range.

Elements	Mean ± SD (K)	Median ± IQR (K)	Min – max (K)
Ground	310.0 ± 0.3	309.9 ± 0.5	309.6–310.5
Vegetation	306.2 ± 0.1	306.2 ± 0.1	306.0–306.5

Table 7
Temperature statistics of the sparsely distributed trees scene. SD: standard deviation. IQR: interquartile range.

Elements	Mean ± SD (K)	Median ± IQR (K)	Min – max (K)
Ground	310.0 ± 0.0	310.0 ± 0.0	309.8–310.0
Vegetation	306.9 ± 0.1	306.9 ± 0.1	306.7–307.1

vegetation emissivity map of the maize scene. The ground emissivity map is generally uniform. At the initial growth period, the vegetated plot exhibits a colour nearly identical to the three bare ground plots. As the vegetation becomes denser (*i.e.*, second and third growth periods), pixel colors significantly diverge from their surroundings. This suggests that retrieving emissivity and temperature from the ground under dense vegetation poses a challenge due to its weak signal.

Fig. 10 shows RGB false colour composites of the retrieved ground and vegetation emissivity map of the forest scene. The ground emissivity map is generally uniform; however, the colors of pixels with sparsely distributed trees differ slightly from the surrounding colors, suggesting that the architecture of tree canopy complicates the separation of temperature and emissivity process.

Fig. 11 shows the retrieved maps of ground and vegetation temperatures of the homogeneous maize canopy. The unmixed component temperature maps for ground and vegetation are distinct, suggesting a feasible temperature separation between vegetation and ground. The retrieved temperature exhibits uniformity across the map, with a standard deviation around 0.3 K and an interquartile range around 0.5 K for ground and around 0.1 K (standard deviation and interquartile range) for vegetation (Table 6). The temperature phenomena contradict established environmental patterns, as vegetation typically reduces soil temperature by intercepting solar radiation that would otherwise reach the ground directly. In our study with simulated data, soil and vegetation temperatures were set as constant across the entire image. Therefore, the observed temperature differences between vegetated and bare soil areas can be attributed to limitations in our inversion algorithm. Analysis of the radiance image reveals that pixels at vegetation-bare soil interfaces exhibit higher radiance values compared to pixels in the center of bare soil areas, due to additional radiation reflected from adjacent vegetation. Consequently, when processed through the Temperature-Emissivity Separation (TES) method, these interface pixels yield higher Land Surface Temperature (LST) values. These pixels are subsequently classified as pure pixels, and their values are used as initial parameters for mixed pixels (soil under vegetation). Although iterative corrections are implemented to minimize these discrepancies, complete temperature uniformity is not achieved.

Fig. 12 shows the retrieved ground and vegetation temperature maps of the arid forest canopy. The unmixed component temperature maps of the ground and vegetation are distinct, indicating that temperature separation between vegetation and ground is feasible. The retrieved temperatures exhibit uniformity across the map, with the standard deviation and interquartile range of soil temperature being almost 0.0 K, and the standard deviation and interquartile range of vegetation temperature being approximately 0.1 K (Table 7).

3.1.2. Quantitative accuracy assessment

TRUST-DART accuracy is quantitatively described using the absolute values of residual error. Two statistical parameters, median and mean error, are used to indicate error variation across iterations. For the maize scene (Fig. 13), although the median and mean errors of radiance and the median error of emissivity consistently decrease with iteration, the mean error of emissivity and median or mean error of temperature may decrease or increase (depending on the bands and components). One explanation is that due to weaker signals, the temperature and emissivity errors of those low-contribution components may increase with iteration, but their impact on the overall pixel radiance is relatively small.

Upon reaching the final iteration, the residual errors in radiance for each component are as follows: for the ground, the mean is 0.08 W/(m^2·sr), and the median is 0.08 W/(m^2·sr); for vegetation, the mean is 0.08 W/(m^2·sr), and the median is 0.10 W/(m^2·sr). The residual errors in emissivity for each component are: for the ground, the mean is 0.036 with a median of 0.037; and for vegetation, the mean is 0.026 with a median of 0.002. The residual errors in temperature for each component are: for the ground, the mean is 1.7 K with a median of 1.8 K; for vegetation, the mean is 0.6 K, with a median of 0.6 K.

For the arid forest scene (Fig. 14), since the facets comprising the canopy and grassland dominate the scene, there are almost no pure pixels, and the gradient differences between pixels are minimal, adding challenges for multiple pixel methods. As a result, the differential radiative transfer equation has stronger linear correlations, making the efficiency of TRUST-DART weaker than in the maize scene, with convergence occurring earlier during iterations. Errors remain stable or decrease with iteration, except for the mean error of ground temperature that increases with iteration.

Upon reaching the final iteration, the residual errors in radiance for each component are as follows: for the ground, the mean is 0.05 W/(m^2·sr), and the median is 0.05 W/(m^2·sr); for vegetation, the mean is 0.05 W/(m^2·sr), and the median is 0.05 W/(m^2·sr). The residual errors in emissivity for each component are: for the ground, the mean is 0.036, and the median is 0.036; for vegetation, the mean is 0.020, and the median is 0.021. The residual errors in temperature for each component are: for the ground, the mean is 1.7 K, and the median is 1.7 K; for vegetation, the mean is 1.3 K, and the median is 1.3 K.

3.2. Application to urban scenes

TRUST-DART accuracy was evaluated using pseudo-ASTER images simulated by DART (see Section 3.2.1), ASTER images (see Section 3.2.2), and *in situ* water body temperature measurements (see Section 3.2.3).

3.2.1. Accuracy assessment with pseudo-ASTER images

3.2.1.1. Visual accuracy assessment. Figs. 15 and 16 show RGB false colour composites of the retrieved component emissivity for Basel and Brussels, respectively, showing distinct colors and good spatial

Table 8
Summary statistics of the retrieved temperature (K) of the pseudo-ASTER Basel image. SD: standard deviation. IQR: interquartile range.

Elements	Mean ± SD (K)	Median ± IQR (K)	Min – max (K)
Ground	311.0 ± 0.2	311.0 ± 0.2	310.4–311.7
Building	303.6 ± 0.1	303.6 ± 0.1	302.9–304.0
Vegetation	307.0 ± 0.1	307.0 ± 0.2	306.5–307.2
Water	302.5 ± 0.2	302.5 ± 0.2	301.8–303.0

Table 9
Summary statistics of the retrieved temperature (K) of the pseudo-ASTER Brussels image. SD: standard deviation. IQR: interquartile range.

Elements	Mean ± SD (K)	Median ± IQR (K)	Min – max (K)
Ground	310.9 ± 0.2	310.9 ± 0.1	305.2–312.2
Building	303.3 ± 0.2	303.3 ± 0.2	302.2–304.6
Vegetation	307.2 ± 0.2	307.3 ± 0.1	305.7–307.8
Water	302.5 ± 0.3	302.6 ± 0.4	301.2–303.2

consistency across all maps. Notably, vegetation has a weaker spatial consistency (Figs. 15c and 16c) than other components. Figs. 17 and 18 show the retrieved component temperatures for Basel and Brussels, with summary statistics in Tables 8 and 9, respectively, and the temperature maps also show distinct colors and consistent spatial patterns.

3.2.1.2. Quantitative accuracy assessment. The quantitative assessment of TRUST-DART accuracy is based on the absolute value of residual error, with error distribution across iterations characterized by median and mean values (Fig. 19 for Basel and Fig. 20 for Brussels). Radiance and most temperature errors decrease with iterations, while emissivity error varies. This mixed behavior is likely due to emissivity's dual role in controlling both emitted and reflected radiance. Indeed, reducing emissivity decreases emitted radiance but increases reflected radiance, complicating its gradient calculation. Consequently, emissivity retrieval is more challenging than temperature retrieval, which depends solely on emitted radiance. For example, the study (Liu et al., 2020) already noted that emissivity is less sensitive in TIR unmixing, further complicating its retrieval.

For Basel, at the inversion final iteration, radiance residual errors for each component averaged over all bands are around 0.03 W/(m^2·sr) (mean) and 0.03 W/(m^2·sr) (median) for buildings, 0.03 W/(m^2·sr) (mean) and 0.02 W/(m^2·sr) (median) for ground, 0.03 W/(m^2·sr) (mean) and 0.02 W/(m^2·sr) (median) for vegetation, and 0.02 W/(m^2·sr) (mean) and 0.01 W/(m^2·sr) (median) for water. The emissivity residual errors for each component averaged over all bands are around 0.048 (mean) and 0.048 (median) for buildings, 0.012 (mean) and 0.012 (median) for ground, 0.019 (mean) and 0.018 (median) for vegetation, and 0.004 (mean) and 0.001 (median) for water. The temperature residual errors for each component are 1.3 K (mean) and 1.3 K (median) for buildings, 0.7 K (mean) and 0.7 K (median) for ground, 1.3 K (mean) and 1.3 K (median) for vegetation, and 0.1 K (mean) and 0.1 K (median) for water.

For Brussels, at the final iteration, the radiance residual errors for each component averaged over all bands are around 0.04 W/(m^2·sr) (mean) and 0.03 W/(m^2·sr) (median) for buildings, 0.04 W/(m^2·sr) (mean) and 0.03 W/(m^2·sr) (median) for ground, 0.04 W/(m^2·sr) (mean) and 0.03 W/(m^2·sr) (median) for vegetation, and 0.04 W/(m^2·sr) (mean) and 0.01 W/(m^2·sr) (median) for water. The emissivity residual errors for each component averaged over all bands are around 0.039 (mean) and 0.041 (median) for buildings, 0.012 (mean) and 0.006 (median) for ground, 0.021 (mean) and 0.013 (median) for vegetation, and 0.019 (mean) and 0.010 (median) for water. The temperature residual errors for each component are 1.6 K (mean) and 1.6 K (median) for buildings, 0.8 K (mean) and 0.7 K (median) for ground, 1.6 K (mean) and 1.6 K (median) for vegetation, and 0.3 K (mean) and 0.1 K (median) for water.

Table 10
Summary statistics of temperature (K) of Basel ASTER image. SD: standard deviation. IQR: interquartile range.

Elements	Mean ± SD (K)	Median ± IQR (K)	Min – max (K)
Ground	293.3 ± 0.6	293.4 ± 0.8	291.1–294.8
Building	293.5 ± 0.4	293.6 ± 0.6	292.2–294.7
Vegetation	292.7 ± 0.2	292.7 ± 0.3	292.4–293.2
Water	294.8 ± 0.3	294.8 ± 0.5	293.7–295.7

Table 11
Summary statistics of temperature (K) of Brussels ASTER image. SD: standard deviation. IQR: interquartile range.

Elements	Mean ± SD (K)	Median ± IQR (K)	Min – max (K)
Ground	283.3 ± 0.6	283.5 ± 1.0	281.5–285.5
Building	282.0 ± 0.8	281.9 ± 1.3	279.0–284.3
Vegetation	283.7 ± 0.5	283.8 ± 0.9	282.9–286.7
Water	285.6 ± 1.2	285.6 ± 2.0	282.3–290.4

3.2.2. Accuracy assessment with ASTER image

3.2.2.1. Visual accuracy assessment. Figs. 21 and 22 show RGB false colour composites of the ASTER and DART images for Basel and Brussels, simulated using temperature and emissivity from TRUST-DART. Although both images are similar, the DART image is sharper and more homogeneous with fewer dispersed dark or bright pixels. This is likely due to the sensor modulation transfer function effect and uncorrected atmospheric effects in the ASTER image, as well as TRUST-DART's assumption that the same components in a sampling window share identical emissivity and temperature.

Figs. 23 and 24 show RGB false composites of the Basel and Brussels component emissivity from ASTER, revealing highly homogeneous maps that align with the geostatistical view that similar components share comparable optical properties at close range. In contrast, vegetation (notably in Basel) shows disconnected patch effects due to weak signals, indicating the challenge of emissivity retrieval. Although previous studies (Gustafson et al., 2006; Hook, 2011) reported step discontinuities in ASTER's LSE products, the component emissivity maps from TRUST-DART are markedly more homogeneous, mitigating these discontinuities compared to TES-derived LST and LSE (Figs. 7 and 8).

Figs. 25 and 26 show the component temperatures of Basel and Brussels from the ASTER image, with summary statistics in Tables 10 and 11. Water has the highest night-time temperatures (*i.e.*, 294.8 K in Basel and 285.8 K in Brussels), owing to its superior specific heat capacity. Additionally, downtown areas have higher temperatures than surrounding rural regions, confirming the reliability of the retrieved emissivity and temperature data.

We observe an unusual temperature pattern in Basel and Brussels. In Basel, vegetation is cooler than buildings, consistent with its lower thermal mass, higher evapotranspiration, and radiative cooling. In Brussels, however, nighttime ASTER and ECOSTRESS radiance images reveal that dense vegetation areas (especially in the southeast) have higher temperatures than downtown urban areas. Additional nighttime ASTER imagery confirms that forested regions consistently have higher radiance than urban areas. We interpret this phenomenon as region-specific, likely caused by cold-air pooling in Brussels' low-lying downtown, where denser, colder air accumulates, and by the effect of the dense vegetation canopy acting as a thermal cover that reduces heat loss, in contrast to the wide urban street that promotes efficient radiative cooling.

3.2.2.2. Quantitative accuracy assessment. Fig. 27 shows the median and mean error variations over iterations for Basel images, while Fig. 28 shows the corresponding data for Brussels. Both cities display a consistent decrease in errors across all bands over iterations. Longer

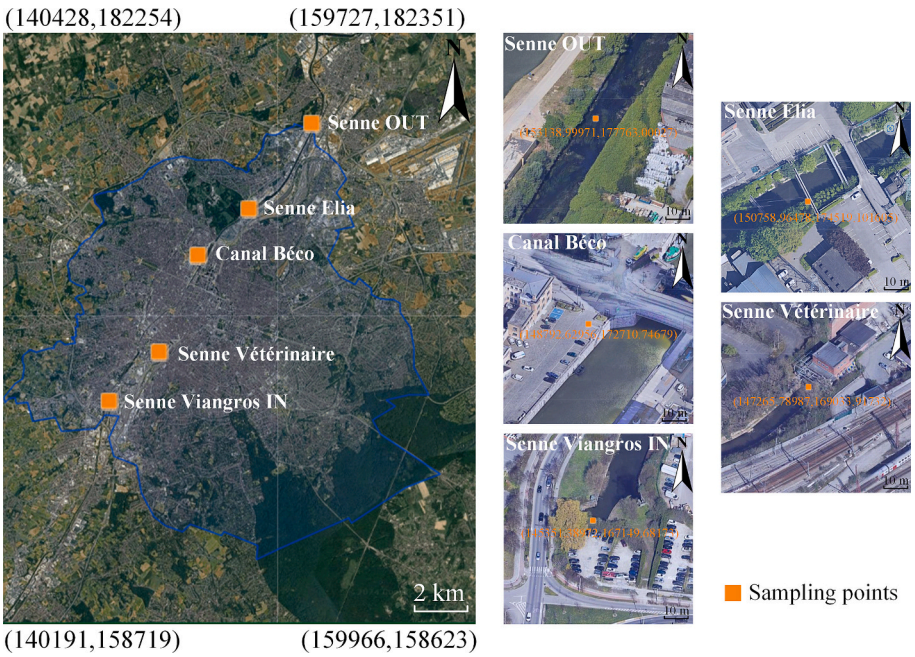

Fig. 6. The location of the field sampling stations. *In situ* measured water temperature from five HYDRIA stations along Senne and Canal are used. The coordinates in the image are in Belgian Lambert 1972 (EPSG: 31370, unit: m). The base satellite images are from HYDRIA (https://hydria.be/fr/carte-interactive-des-sites/).

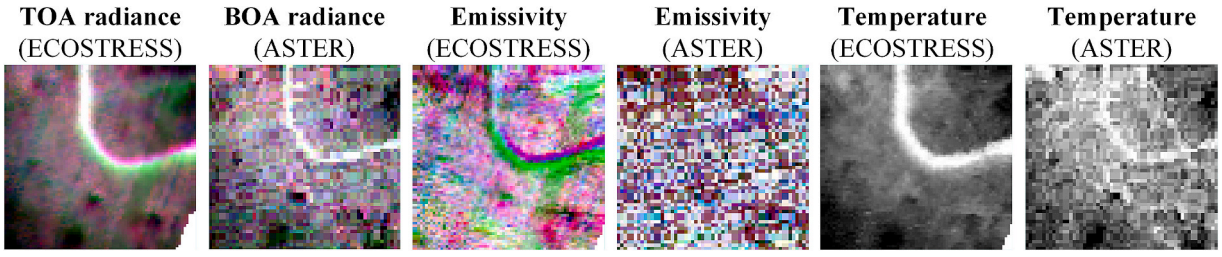

Fig. 7. The ASTER and ECOSTRESS images over Basel. The radiance image and emissivity map are false RGB compositions, and the temperature map is a single-band display. The RGB composite images are generated using the following spectral bands: Red (ASTER B14; ECOSTRESS B5) corresponding to wavelengths of 11.300 μm (ASTER) and 12.001 μm (ECOSTRESS), Green (ASTER B12; ECOSTRESS B3) corresponding to wavelengths of 9.100 μm (ASTER) and 9.060 μm (ECOSTRESS), and Blue (ASTER B10; ECOSTRESS B1) corresponding to wavelengths of 8.300 μm (ASTER) and 8.285 μm (ECOSTRESS). Owing to the orbital observation coverage, ECOSTRESS data misses a small part of the data at the right-bottom corner. The phenomenon of registration error is observed in ECOSTRESS images. (For interpretation of the references to colour in this figure legend, the reader is referred to the web version of this article.)

wavelengths (10.6 μm and 11.3 μm) exhibit lower radiance errors, likely due to high atmospheric transmittance and stable emissivity (Tonooka, 2005). Shorter wavelengths (8.3 μm, 8.65 μm, and 9.1 μm) show higher errors, attributed to silicate absorption and water vapor interference (Gillespie et al., 1998; Tonooka, 2005). Notably, these variations are absent in the simulated data, which reflect ideal experimental conditions.

At the final iteration for Basel, the average radiance residual errors over all bands are around 0.06 W/(m^2·sr) (mean) and 0.03 W/(m^2·sr) (median) for buildings, ground, and vegetation, and 0.09 W/(m^2·sr) (mean) and 0.06 W/(m^2·sr) (median) for water. For Brussels, the corresponding values are around 0.18 W/(m^2·sr) (mean) and 0.05 W/

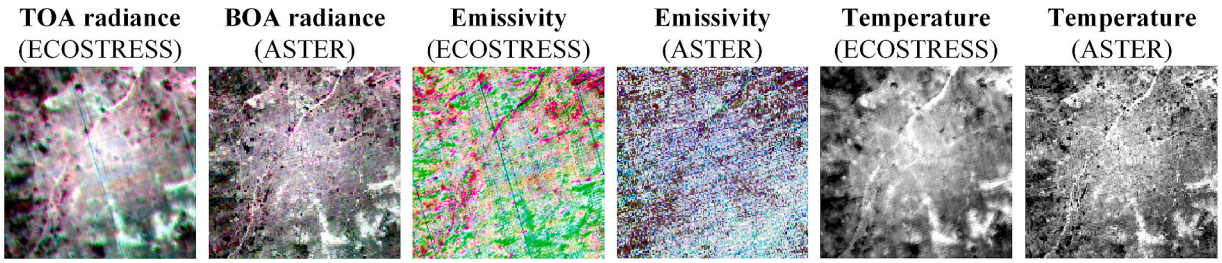

Fig. 8. The ASTER and ECOSTRESS images over Brussels. Radiance image and emissivity maps are false RGB compositions, and the temperature map is a single-band display. The RGB composite images are generated using the following spectral bands: Red (ASTER B14; ECOSTRESS B5) corresponding to wavelengths of 11.300 μm (ASTER) and 12.001 μm (ECOSTRESS), Green (ASTER B12; ECOSTRESS B3) corresponding to wavelengths of 9.100 μm (ASTER) and 9.060 μm (ECOSTRESS), and Blue (ASTER B10; ECOSTRESS B1) corresponding to wavelengths of 8.300 μm (ASTER) and 8.285 μm (ECOSTRESS). The phenomenon of registration error is observed in ECOSTRESS images. (For interpretation of the references to colour in this figure legend, the reader is referred to the web version of this article.)

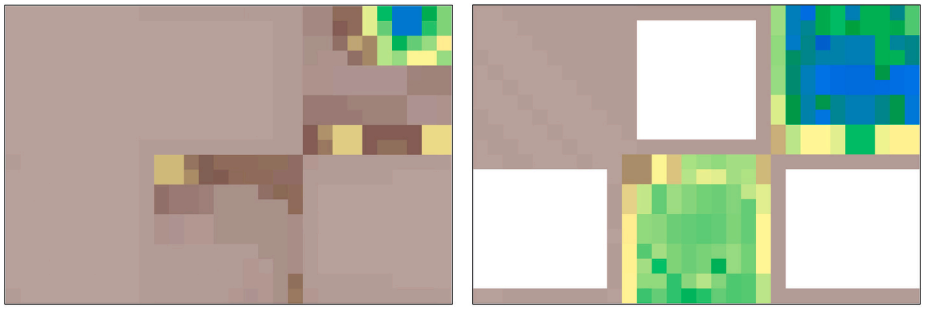

Fig. 9. The ground and vegetation emissivity maps of the maize scene using RGB false colour composition. (a) Ground emissivity. (b) Vegetation emissivity. The RGB images are composed using bands B14 (Red), B12 (Green), and B10 (Blue), corresponding to wavelengths 11.3, 9.1, and 8.3 μm, respectively. (For interpretation of the references to colour in this figure legend, the reader is referred to the web version of this article.)

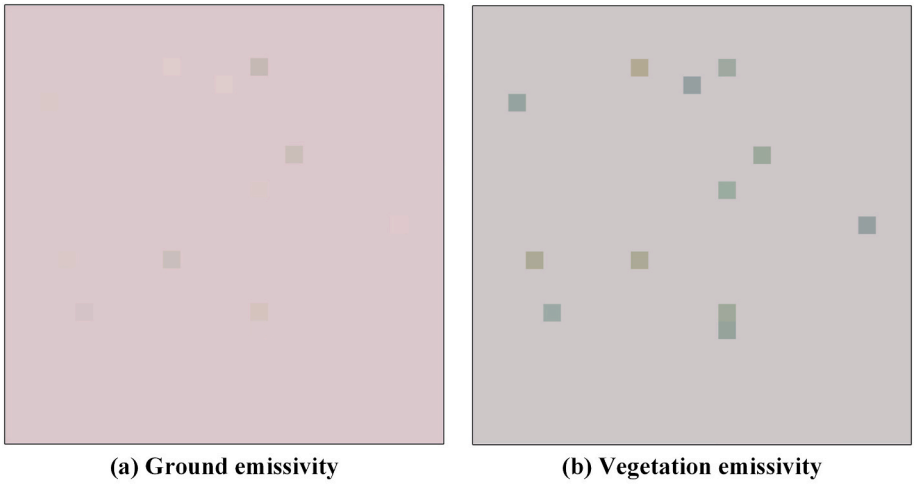

Fig. 10. The ground and vegetation emissivity maps of the arid forest scene using RGB false colour composition. (a) Ground emissivity. (b) Vegetation emissivity. The RGB images are composed using bands B14 (Red), B12 (Green), and B10 (Blue), corresponding to wavelengths 11.3, 9.1, and 8.3 μm, respectively. (For interpretation of the references to colour in this figure legend, the reader is referred to the web version of this article.)

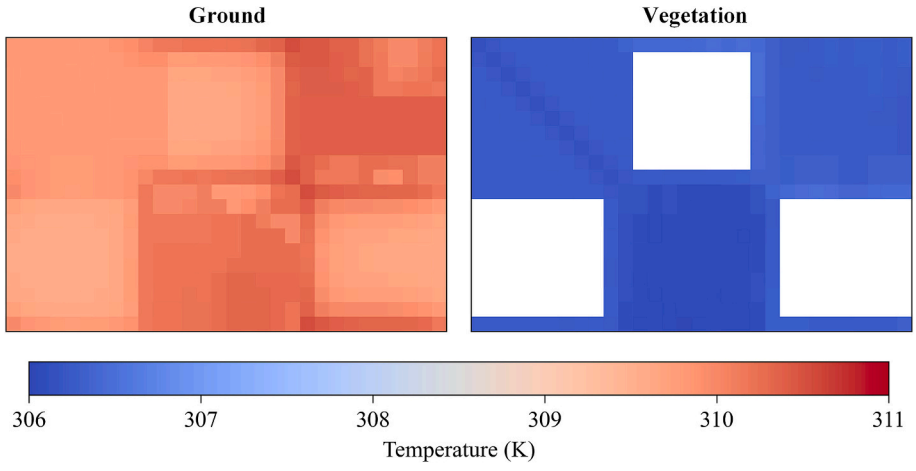

Fig. 11. The maize scene temperature maps. The pixels that appear missing represent areas where the component fraction of the specified land surface type is negligible.

(m^2·sr) (median) for buildings, 0.26 W/(m^2·sr) (mean) and 0.06 W/(m^2·sr) (median) for ground, 0.13 W/(m^2·sr) (mean) and 0.07 W/(m^2·sr) (median) for vegetation, and 0.35 W/(m^2·sr) (mean) and 0.08 W/(m^2·sr) (median) for water. The lower accuracies for water likely stem from the PPS module due to the TES method's pure pixel requirement, though this had minimal impact given water's limited presence and few mixed pixels in the urban area.

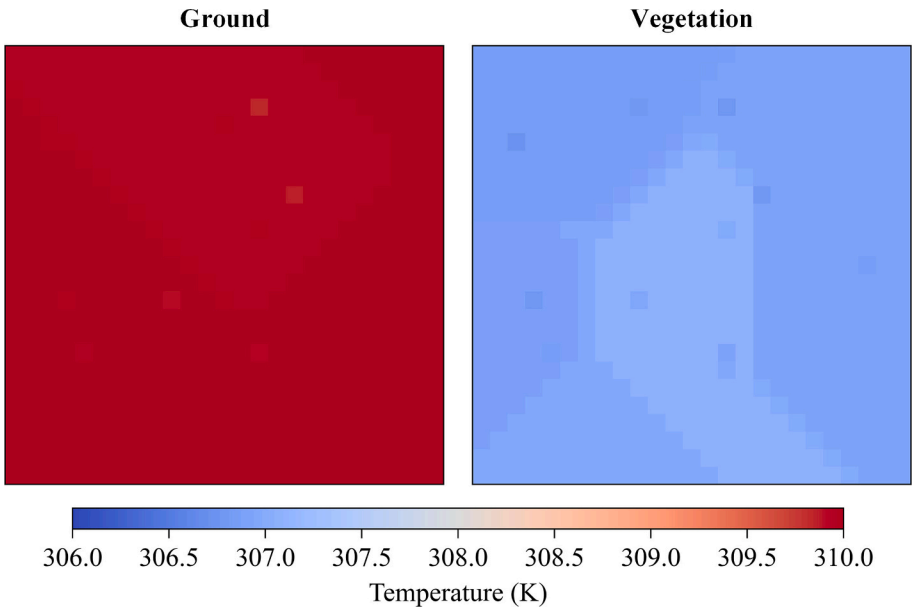

Fig. 12. The temperature maps of the sparsely distributed trees scene.

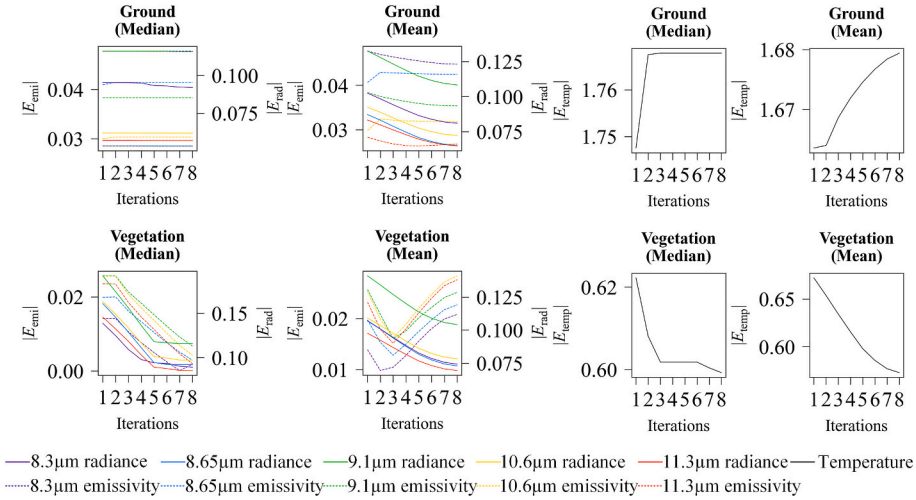

Fig. 13. Evaluation of component temperature, emissivity, and pixel radiance accuracy using median and mean residual error in the maize scene. A pixel is categorized as belonging to a particular class if it contains the corresponding component. Consequently, a single pixel may be included in multiple component classifications. $|E_{\text{temp}}|$: Absolute residual error of temperature (K); $|E_{\text{emi}}|$: Absolute residual error of emissivity (unitless); $|E_{\text{rad}}|$: Absolute residual error of radiance [W/(m^2·sr)].

3.2.3. *Accuracy assessment with in situ water body temperature*

Fig. 29 compares three measurements (ASTER LST, the TRUST-DART component temperature, and *in situ* water temperature) in Brussels. TRUST-DART's component temperature is lower than ASTER LST in Senne OUT, Senne Elia, Senne Vétérinaire, and Senne Viangros IN, while Canal Béco shows identical values. Fig. 6 indicates that the station's location deviates slightly from the river surface. Cross-referencing ASTER and PlanetScope images based on coordinates reveals that the pixel contains very little water component, resulting in poor unmixing. An adjacent eastern pixel shows an ASTER LST of 295.2 K *versus* 294.1 K from TRUST-DART.

Three factors explain why the water component temperatures retrieved by TRUST-DART are higher than *in situ* measurements. First, *in situ* measurements reflect the water body temperature, while remote sensing captures the typically higher surface temperature, especially at midday. Second, the ASTER LST product may be overestimated, as shown in Appendix A, where ASTER LST exceeds ECOSTRESS LST for the same period, and the accuracy of the initial LST significantly affects TIR unmixing (Liu et al., 2020). Third, validating component temperatures with measured data is challenging (Bian et al., 2020) due to discrepancies between point-based and area-based measurements (Bian et al., 2016; Liu et al., 2020).

4. Discussion and conclusions

4.1. *Discussion*

4.1.1. *Advantages*

The TRUST-DART methodology advances ASTER's traditional TES approach by retrieving component thermodynamic temperatures and emissivity values rather than producing aggregate measurements. Component-specific measurements are critical for vegetation and urban studies to provide insights into plant physiology, environmental responses, and evapotranspiration modeling, whereas ASTER-derived LSE

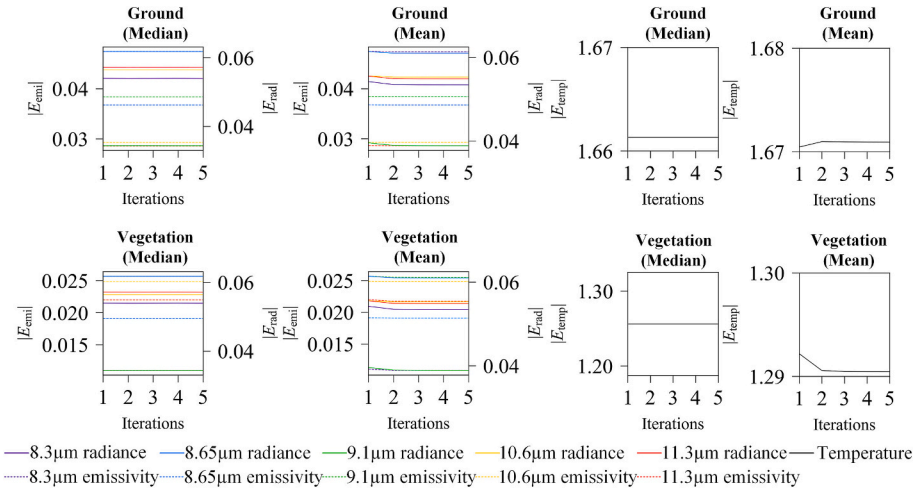

Fig. 14. Evaluation of component temperature, emissivity, and pixel radiance accuracy using median and mean residual error in the arid forest scene. A pixel is categorized as belonging to a particular class if it contains the corresponding component. Consequently, a single pixel may be included in multiple component classifications. $|E_{\text{temp}}|$: Absolute residual error of temperature (K); $|E_{\text{emi}}|$: Absolute residual error of emissivity (unitless); $|E_{\text{rad}}|$: Absolute residual error of radiance [W/(m^2·sr)].

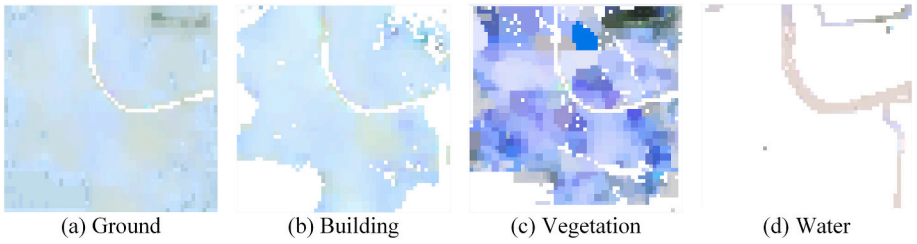

Fig. 15. False RGB compositions of the retrieved component emissivity of the four elements in Basel. (a) Ground. (b) Building. (c) Vegetation. (d) Water. They are from bands B14 (Red), B12 (Green), and B10 (Blue) at wavelengths 11.3, 9.1, and 8.3 μm, respectively. White pixels (*i.e.*, no value) indicate areas with a negligible component fraction of the given scene element. The left bottom blank in the building and vegetation are due to the missing data (administrative problem).(For interpretation of the references to colour in this figure legend, the reader is referred to the web version of this article.)

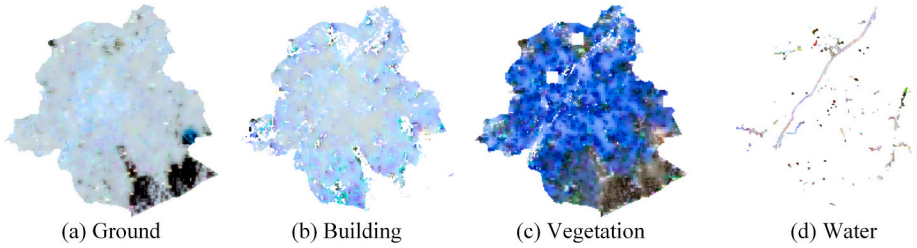

Fig. 16. False RGB compositions of the retrieved component emissivity of the four elements in Brussels. (a) Ground. (b) Building. (c) Vegetation. (d) Water. They are from bands B14 (Red), B12 (Green), and B10 (Blue) at wavelengths 11.3, 9.1, and 8.3 μm, respectively. White pixels show areas with a negligible component fraction of the given scene element. The blank squares in the vegetation are due to the missing tree data (administrative problem). (For interpretation of the references to colour in this figure legend, the reader is referred to the web version of this article.)

and LST products offer integrated averages that limit such detailed analysis. In addition, these component maps integrate seamlessly into DART, facilitating radiative transfer and radiation budget simulations at any desired spatial resolution.

Previous studies have explored individual strategies, for example, using digital surface models for nonlinear analyses (Fontanilles and Briottet, 2011) or employing land cover classification maps (Mitraka et al., 2012), for TIR unmixing. However, the combined application of these approaches, referred to as tagged mock-ups, remains underexplored. TRUST-DART leverages tagged mock-ups to reduce unknowns in TIR unmixing models by eliminating the endmember identification step and replacing abundance estimation with gradients derived from radiative transfer. These gradients, which incorporate three-dimensional structural information, more accurately quantify the radiative contributions of components. As a result, TRUST-DART directly derives the thermodynamic temperature of components, unlike abundance-based methods (*e.g.*, TRUST and TRUST-DNS) that estimate component LST. Furthermore, in contrast to a deep learning method (Wang et al., 2024a), TRUST-DART's gradients propagate among parameters with explicit physical meaning, enhancing their interpretability.

TRUST-DART simultaneously separates component temperature and emissivity without requiring prior emissivity knowledge, which is a significant advantage since few TIR unmixing methods can achieve this,

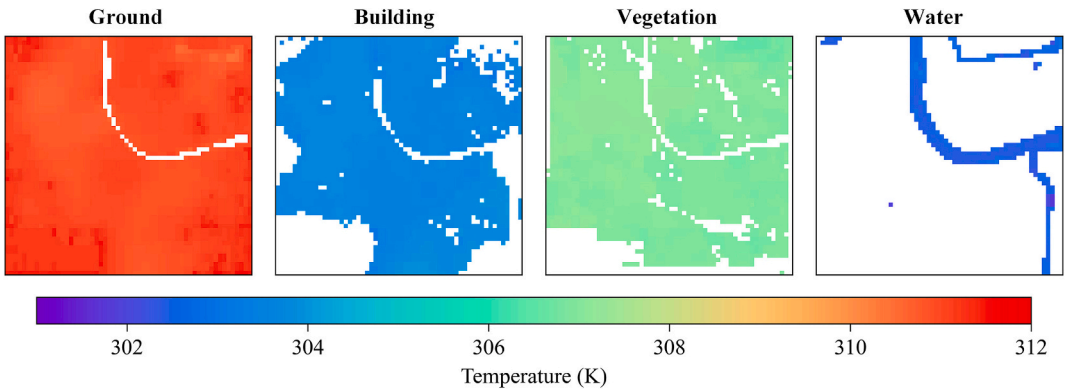

Fig. 17. Temperature maps of the four elements retrieved from the Basel pseudo-ASTER image. White pixels show areas with a negligible component fraction of the given scene element. The left bottom blank in the building and vegetation are due to the missing data (administrative problem).

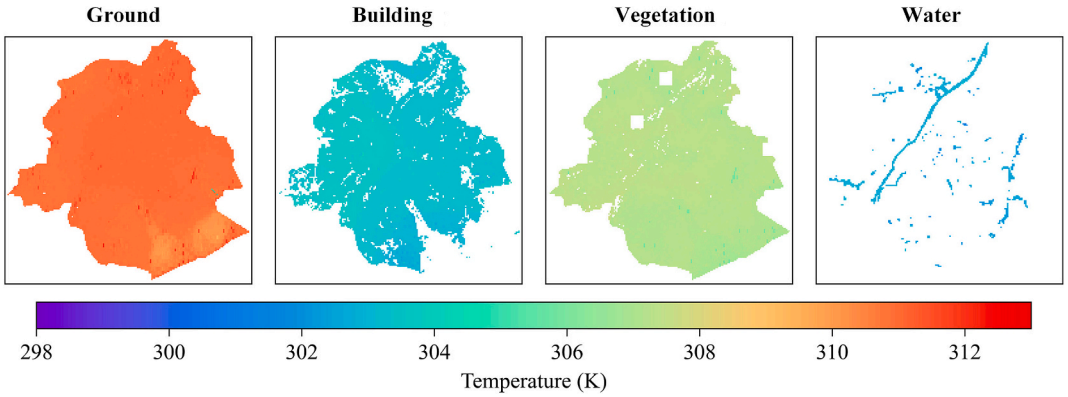

Fig. 18. Temperature maps of the four elements retrieved from the Brussels pseudo-ASTER image. White pixels show areas with a negligible component fraction of the given scene element. The blank squares in the vegetation are due to the missing tree data (administrative problem).

and obtaining accurate LSE in advance is often challenging. A 0.01 LSE error can induce roughly a 0.6 K error in LST (Jiménez-Muñoz and Sobrino, 2003), underscoring the impact of LSE inaccuracies in non-simultaneous methods. Moreover, while some studies (Cubero-Castan et al., 2014; Granero-Belinchon et al., 2020) use pure pixel LSE as a proxy for component emissivity, they neglect its spatial variability, and it is an aspect our results indicate may have potential for further refinement.

TRUST-DART requires much less stringent image resolution than its counterparts. For example, TRUST fails with resolutions coarser than 1 m and fewer than 30 bands, while TRUST-DNS requires resolutions finer than 8 m, at least 8 bands, and both daytime and nighttime images (imposing strict revisit cycle constraints), and these requirements are even challenging for future Thermal Infra-Red Imaging Satellite for High-resolution Natural Resource Assessment (TRISHNA) satellite (4 bands at 60 m). In contrast, TRUST-DART, which utilizes ASTER images (5 bands at 90 m), operates under significantly relaxed satellite requirements. Table 12 details these usage restrictions. Existing research (Liu et al., 2020) indicates that prior knowledge of temperature differences can enhance unmixing processes. For instance, the SC module exploits such differences (*i.e.*, leveraging relationships between emissivity and temperature) to identify and correct errors in both emissivity and temperature maps. In our simulation, we enforce established temperature constraints: vegetation is set to be cooler than soil in soil-vegetation scenes, while urban scenes follow diurnal patterns where water bodies are cooler during the day and warmer at night. No pixels are flagged as invalid in the SC module in our case since the satellite imagery is carefully chosen to avoid cloud cover and atmospheric interference. Moreover, incorporating additional constraints, such as spectral reflectance shapes, can further improve the SC module's performance.

4.1.2. Limitations and prospects

4.1.2.1. Limitations. TRUST-DART faces limitations due to its reliance on multi-pixel unmixing, which requires adjacent pixels with varying surface parameters. In homogeneous scenes, like the arid forest, the gradients of components from different pixels are almost identical, leading to strong linear correlations that complicate solving the system. Additionally, the distribution of components in pixels affects whether the moving window is solvable, which is uncontrollable. In our studies, 0.00 % of pixels in the maize scene, 0.06 % in Basel, 0.37 % in Brussels, and 7.84 % in the arid forest scene are marked as unresolved pixels by sliding windows in the GI module. The maize scene, with only two distinct components, has the highest proportion of pure pixels, making it the simplest scenario. Basel, with four components, has a higher proportion of pure pixels than Brussels, leading to fewer unstable solutions. In contrast, the arid forest scene, with no pure pixels and a homogeneous grass canopy, results in the highest proportion of unresolved pixels. A potential solution is using a dynamic neighborhood size (Liu et al., 2020). Furthermore, applying autocorrelations of physical properties among neighboring pixels reduces spatial resolution when decomposing component temperatures (Zhan et al., 2013). TRUST-DART cannot distinguish temperature and emissivity variations of a single component within one pixel, as the component temperature may not be isothermal due to illuminated and shadowed areas (Bian et al., 2016). However, for vegetation with dense canopy coverage and high LAI values, the thermal profiles of the foliar layer and substrate soil show similar temperature

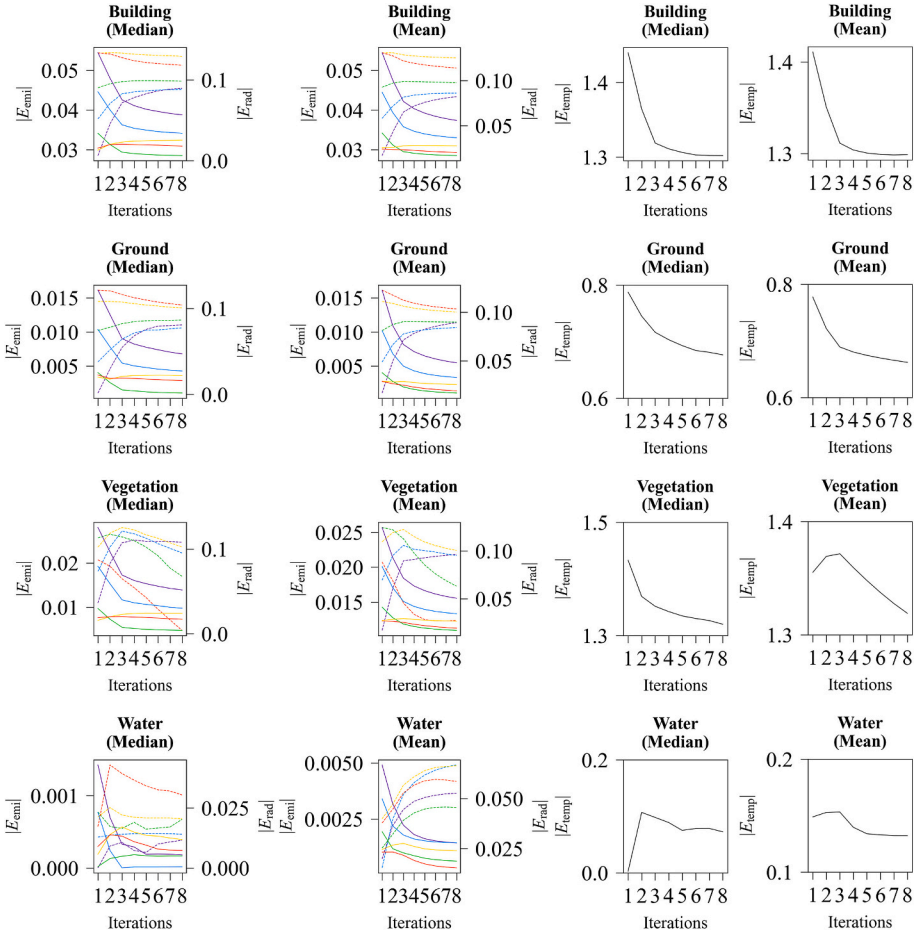

Fig. 19. Basel: accuracy assessment of component temperature, emissivity, and pixel radiance using the median and mean residual error. A pixel belongs to a specific class if it contains the corresponding component. Then, a pixel can be included in multiple component classifications. Absolute residual errors are $|E_{\text{temp}}|$ for temperature (K), $|E_{\text{emi}}|$ for emissivity (unitless), and $|E_{\text{rad}}|$ for radiance [W/(m^2·sr)].

patterns (Francois et al., 1997; Li et al., 2001).

TRUST-DART faces limitations with multi-source data methods due to its use of 3D mock-ups, which can cause geometry misregistration between simulated DART and satellite images, as well as viewing angle variations, leading to errors in estimating gradients and impacting the accuracy of separated component emissivity and temperature. However, the rise of Light Detection and Ranging (LiDAR) technology has made 3D mock-ups more accessible (Ma et al., 2023). Urban 3D mock-ups are now freely accessible through software plugins such as Blender's add-on (https://blender-addons.org/blosm/), which typically remain accurate for several years compared to optical images.

The TRUST-DART method, designed for multi-component analysis in urban areas, addresses the gap in unmixing techniques for deriving thermodynamic temperatures in such environments. It assumes that 3D scenes accurately represent reality, a robust assumption in urban settings due to the stability and geometric regularity of urban structures. Thus, our research focuses on urban scenarios. Applying TRUST-DART to vegetated areas is more challenging, as vegetation canopy structure changes with seasons and growth cycles. In homogeneous scenes, spectral gradient variations between vegetation and soil are similar, increasing the difficulty of mathematical solutions due to potential linear dependence. In heterogeneous scenes, accurate temperature retrieval depends on whether endmember gradients match actual conditions, requiring subpixel-level 3D modeling that must be frequently updated. However, current technology cannot achieve high-frequency, high-precision dynamic 3D modeling of vegetation. Additionally, we did not consider angular effects, commonly used in vegetation unmixing, since ASTER products, which we used, lack observational angle information due to orthorectification. Thus, we assumed a nadir observation for our analysis.

The performance of TRUST-DART in the longwave is less stable than US-DART (Zhen et al., 2025) in the shortwave due to the higher number of unknowns, and the poor stability of the equation system, leading to difficulty in solving the equations system. Additionally, our attempts find that considering the vegetation as a Lambertian plane in the experiments significantly improves the GI module of TRUST-DART.

4.1.2.2. Prospects. Although TRUST-DART uses the TES method, the LST and LSE are required in the PPS module and can be derived from various methods beyond TES. This flexibility enables TRUST-DART to evolve with different methods for separating temperature and emissivity and sensors (Michel et al., 2021; Zhou and Cheng, 2020). While the same Maximum-Minimum apparent emissivity Difference (MMD) coefficients of the TES method are currently used for all components, tailored coefficients for specific land-cover types (manmade *vs.* non-manmade) can be applied (Michel et al., 2021), with 3D mock-ups providing the classification data needed for this adjustment.

TRUST-DART faces challenges due to uncorrected atmospheric errors, as it relies on at-surface radiance images. Incorporating the Temperature Retrieval and Surface Emissivity (TRSM) model (Ma et al., 2002) or the DART atmosphere module can help address this. The TRSM model can retrieve temperature, emissivity, and atmospheric profiles from top-of-atmosphere radiance images, allowing TRUST-DART to use more comprehensive data and reduce atmospheric errors.

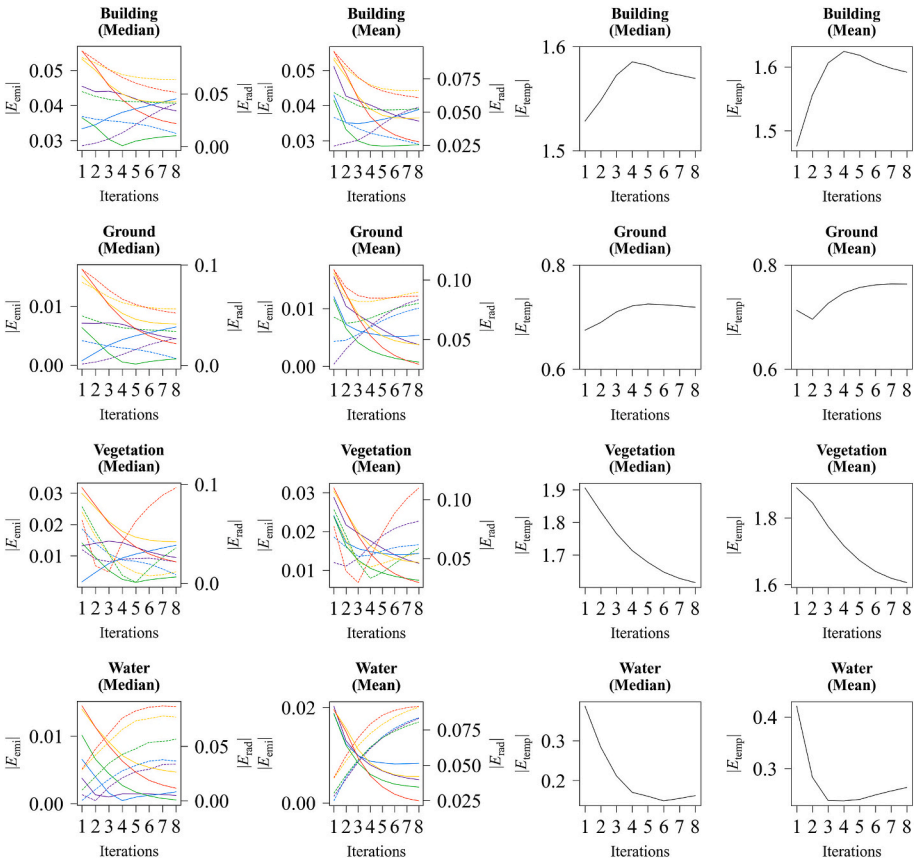

Fig. 20. Brussels: accuracy assessment of component temperature, emissivity, and pixel radiance using the median and mean residual error. A pixel belongs to a specific class if it contains the corresponding component. Then, a single pixel can be included in multiple component classifications. Absolute residual errors are $|E_{temp}|$ for temperature (K), $|E_{emi}|$ for emissivity (unitless), and $|E_{rad}|$ for radiance [W/(m^2·sr)].

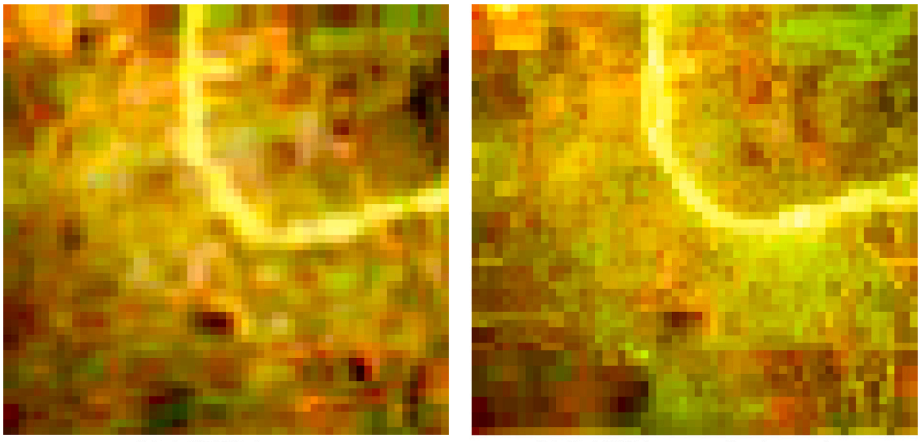

(a) ASTER image (b) DART image after inversion

Fig. 21. Basel: false RGB composition images for bands B14 (Red), B12 (Green), and B10 (Blue), corresponding to wavelengths 11.3, 9.1, and 8.3 μm, respectively. (a) ASTER image; (b) DART image simulated using emissivity and temperature retrieved from TRUST-DART. (For interpretation of the references to colour in this figure legend, the reader is referred to the web version of this article.)

4.2. Conclusions

We propose the TRUST-DART method to separate component emissivity and temperature from TIR multispectral at-surface radiance images. To evaluate its accuracy, we used two scenes (vegetation and urban) and two image types (ASTER and pseudo-satellite images simulated by DART). The residual radiance error is typically around 0.05 W/(m^2·sr). Assuming the co-registration and sensor noise errors are ignored, the median residual error of emissivity is around 0.02, and the median residual error of temperature is around 1 K.

TRUST-DART improves upon existing TIR unmixing methods by enabling simultaneous retrieval and multi-component analysis. However, it may encounter challenges common to multi-pixel and multi-source data models. Future improvements could include incorporating the enhanced TES method, such as using distinct coefficients in the MMD module or top-of-atmosphere radiance images.

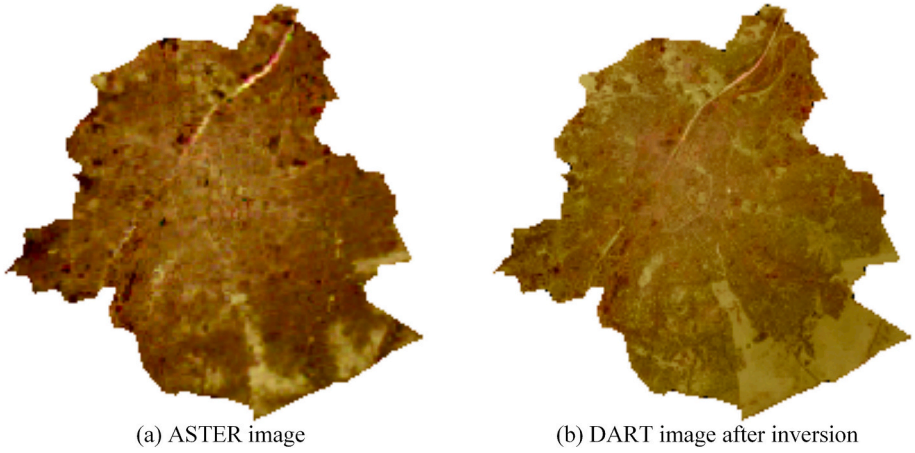

Fig. 22. Brussels: false RGB composition images from bands B14 (Red), B12 (Green), and B10 (Blue), corresponding to wavelengths 11.3, 9.1, and 8.3 μm, respectively. (a) ASTER image; (b) DART image simulated using emissivity and temperature retrieved from TRUST-DART. (For interpretation of the references to colour in this figure legend, the reader is referred to the web version of this article.)

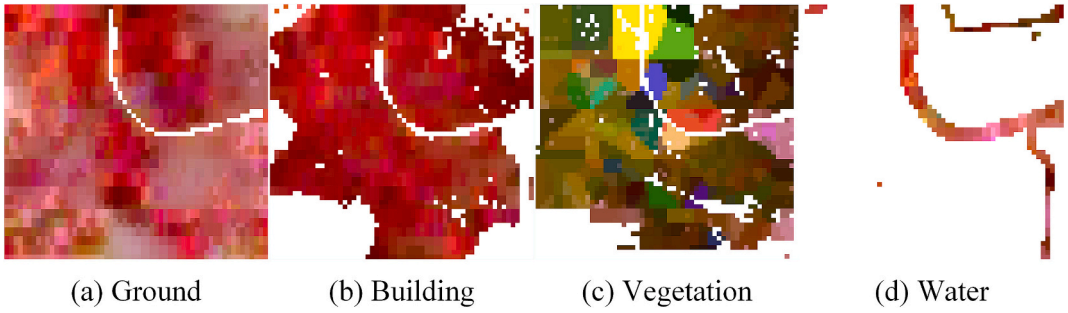

Fig. 23. Basel: false RGB composition of the retrieved emissivity of the four elements. The RGB images are from bands B14 (Red), B12 (Green), and B10 (Blue), corresponding to wavelengths 11.3, 9.1, and 8.3 μm, respectively. (a) Ground. (b) Building. (c) Vegetation. (d) Water. The left bottom blank in the building and vegetation are due to the missing data (administrative problem). (For interpretation of the references to colour in this figure legend, the reader is referred to the web version of this article.)

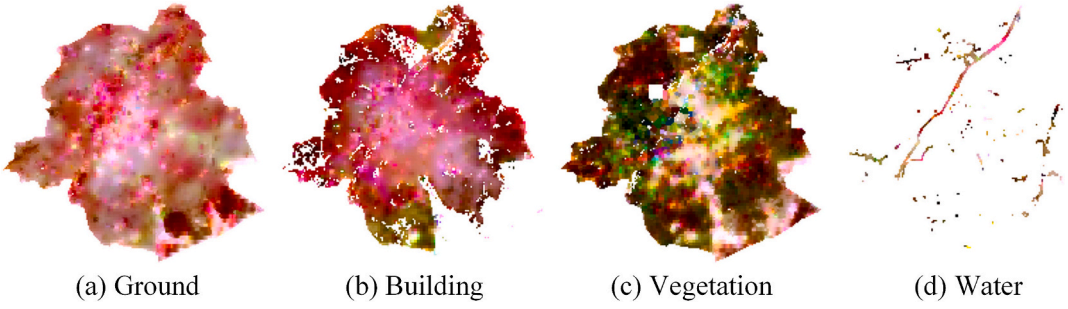

Fig. 24. Brussels: false RGB composition of the retrieved emissivity of the four elements. The RGB images are from bands B14 (Red), B12 (Green), and B10 (Blue), corresponding to wavelengths 11.3, 9.1, and 8.3 μm, respectively. (a) Ground. (b) Building. (c) Vegetation. (d) Water. The blank squares in the vegetation are due to the missing tree data (administrative problem). (For interpretation of the references to colour in this figure legend, the reader is referred to the web version of this article.)

TRUST-DART is compatible with both Windows and Unix platforms and includes a user-friendly graphical interface. The source code is available with the DART model for free at the website (https://dart.omp.eu/#/getDart).

CRediT authorship contribution statement

Zhijun Zhen: Writing – original draft, Methodology, Validation, Funding acquisition, Data curation. **Shengbo Chen:** Supervision, Writing – review & editing, Funding acquisition. **Nicolas Lauret:** Software, Data curation. **Abdelaziz Kallel:** Methodology. **Tiangang Yin:** Writing – review & editing. **Jonathan León-Tavares:** Funding acquisition, Writing – review & editing. **Biao Cao:** Writing – review & editing. **Jean-Philippe Gastellu-Etchegorry:** Conceptualization, Writing – review & editing, Supervision, Funding acquisition.

Declaration of competing interest

The authors declare that they have no known competing financial interests or personal relationships that could have appeared to influence

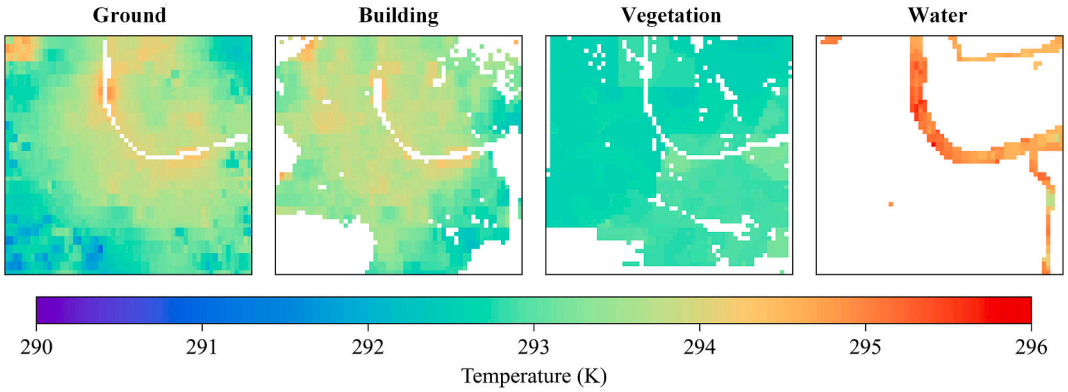

Fig. 25. Basel: temperature maps of the four elements. (a) Ground. (b) Building. (c) Vegetation. (d) Water. The left bottom blank in the building and vegetation are due to the missing data (administrative problem).

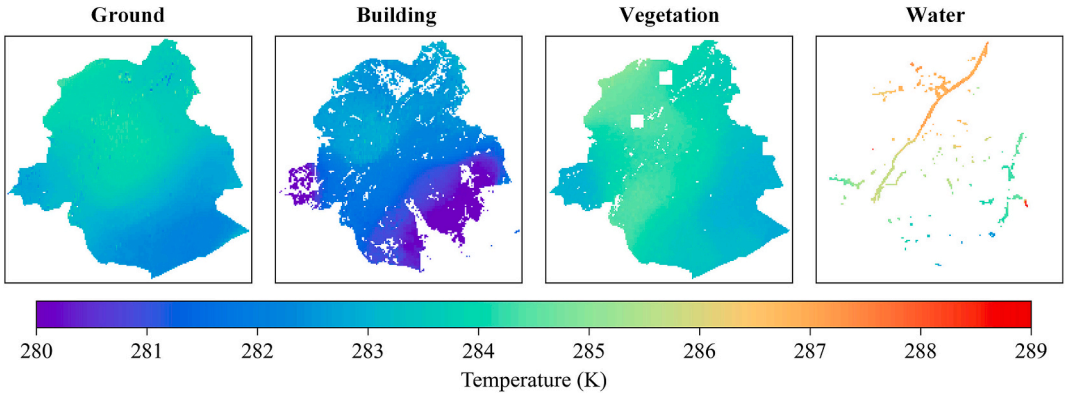

Fig. 26. Brussels: temperature maps of the four elements retrieved. (a) Ground. (b) Building. (c) Vegetation. (d) Water. The blank squares in the vegetation are due to the missing tree data (administrative problem).

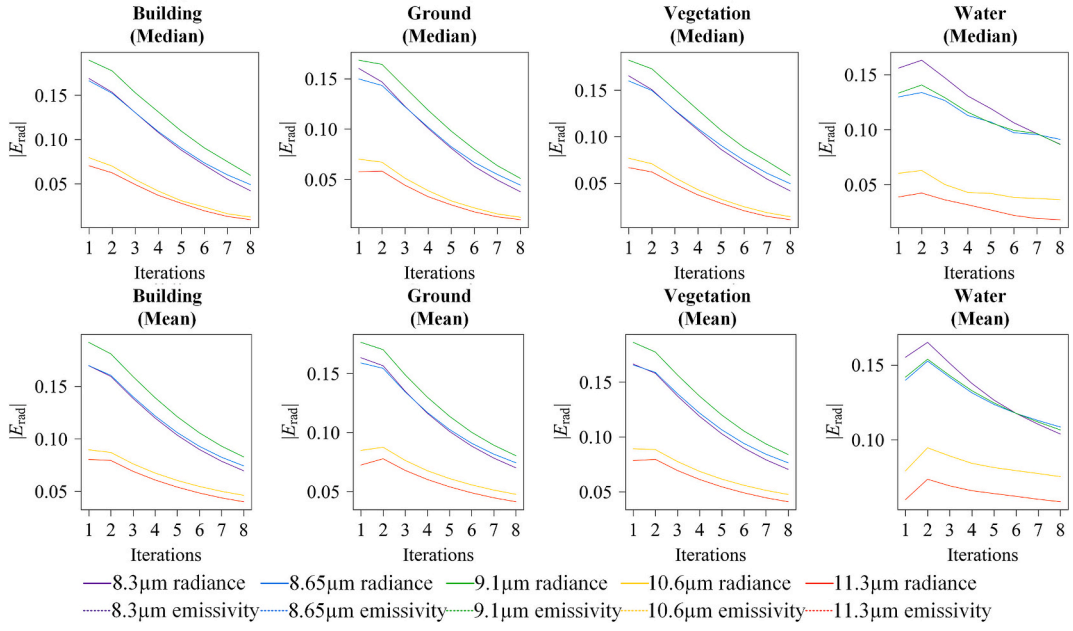

Fig. 27. Basel: evaluation of pixel radiance accuracy using median error indicator (dotted line) and interquartile range (shaded area). A pixel belongs to a particular class if it contains the corresponding component. Then, a single pixel can be included in multiple component classifications. $|E_{rad}|$ is the absolute residual error of radiance [W/(m^2·sr)].

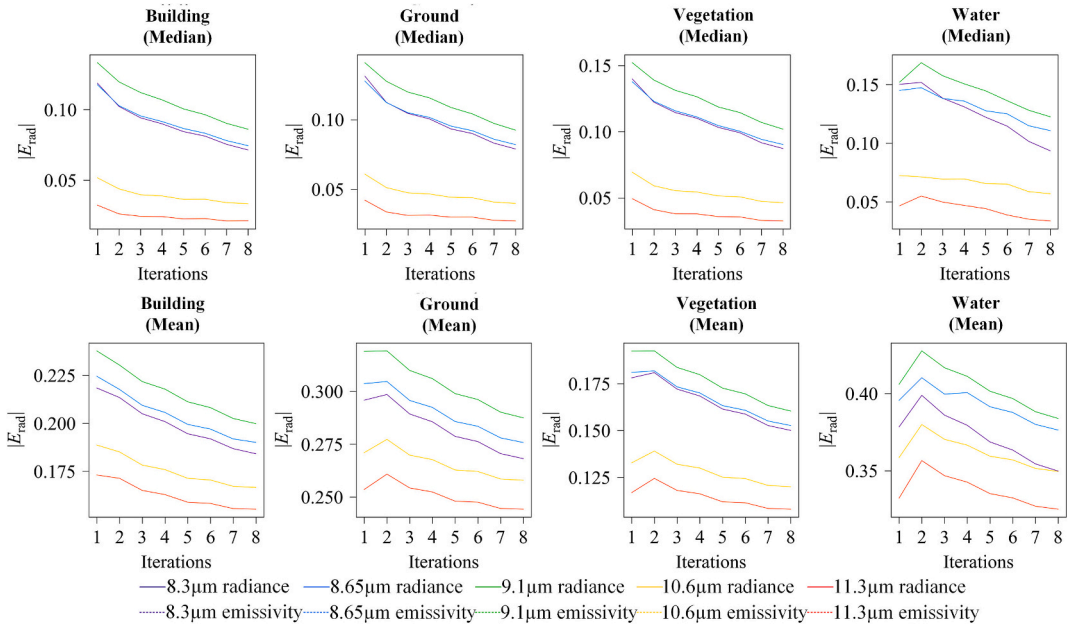

Fig. 28. Brussels: evaluation of pixel radiance accuracy using median error indicator (dotted line) and interquartile range (shaded area). A pixel belongs to a specific class if it contains the corresponding component. Consequently, a single pixel can be included in multiple component classifications. $|E_{rad}|$ is the absolute residual error of radiance [W/(m^2·sr)].

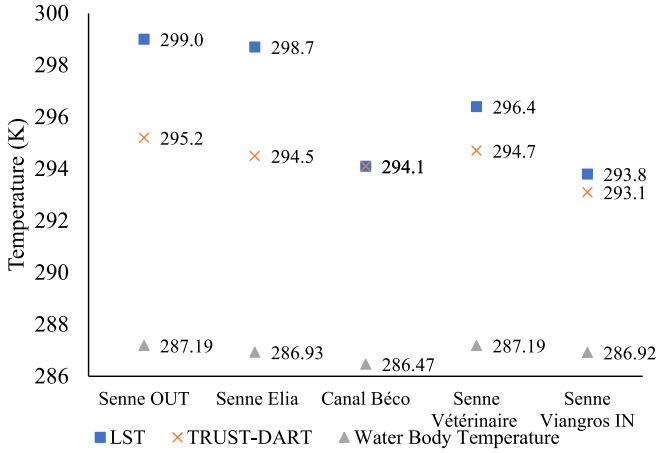

Fig. 29. Comparison of ASTER LST, TRUST-DART, and measured water body temperature in the five sampling sites (Senne OUT, Senne Elia, Canal Béco, Senne Vétérinaire, Senne Viangros IN).

Table 12
Comparisons of restrictions among TRUST, TRUST-DNS, and TRUST-DART.

Evaluations	TRUST	TRUST-DNS	TRUST-DART
Number of bands	30	8	5
Spatial resolution (m)	1	8	90
Component emissivity	Spatial invariance	Spatial invariance	Spatial variance
Component temperature	Spatial variance	Spatial variance	Spatial variance
Simultaneous separation	NO	NO	YES
Application scenes	Small roof	City center	Entire city
Multitemporal images free	YES	NO	YES
Manual operation free	NO	NO	YES
Linearity	Linearity	Linearity	Nonlinearity
3D mock-up free	YES	YES	NO

the work reported in this paper.

Acknowledgments

The authors thank the National Natural Science Foundation of China (NSFC, grant 42201372), the Key Scientific and Technological Initiative for the Satellite and Application of Changchun (No. 2024WX06), the TOSCA program of the French Space Center (CNES), the Belgium Science Policy Office BELSPO STEREO IV Programme (contract SR/67/408), and the National Key Research and Development Program of China (No. 2020YFA0714103).

The authors thank Eric Chavanon and Jordan Guilleux from the University of Toulouse for providing DART software. The authors thank Robbe Neyns from Vrije Universiteit Brussel for providing Brussels' tree geometry and location data. The authors thank Roland Vogt and Christian Feigenwinter from University of Basel for providing Basel's data. The authors thank Lucas Landier from CNES for his innovative ideas on the inversion of satellite images.

This research utilized data provided by NASA and Japan's Ministry of Economy, Trade and Industry (METI) ASTER and NASA's Jet Propulsion Laboratory (JPL) ECOSTRESS. We are grateful for the support and access to these valuable datasets. The authors express their gratitude to the editor and reviewers for their valuable feedback and thorough review of the manuscript.

Appendix A

During our investigation of western Brussels (around 50°50'17.59"N, 4°16'15.09"E), we analyzed three LST images (*i.e.*, two from ECOSTRESS and one from ASTER), and all were acquired within a two-hour window on the same night (Fig. A.1). While the sequential ECOSTRESS images (taken at 19:49:20 and 21:25:32) show the expected pattern of nocturnal cooling (mean temperatures of 280.5 K and 279.5 K respectively), the subsequent ASTER image (taken at 21:26:43) unexpectedly shows higher temperatures (mean temperatures of 281.9 K) than both ECOSTRESS readings (Table A.1). This observation serves as a compelling demonstration of the risks inherent in combining data from

different satellite platforms, even within short temporal windows.

Table A.1
Mean and median temperature of ECOSTRESS and ASTER images at the western areas of Brussels. SD: standard deviation. IQR: interquartile range.

Sensor	ID	Time (UTC)	Temperature (K)
ECOSTRESS	ECOSTRESS_L2_LSTE_01275_002_20180926T194920_0601_03_LST_UTM	2018.09.26 19:49:20	mean ± SD: 280.5 ± 1.1 median ± IQR: 280.5 ± 1.5
ECOSTRESS	ECOSTRESS_L2_LSTE_01276_002_20180926T212532_0601_03_LST_UTM	2018.09.26 21:25:32	mean ± SD: 279.5 ± 1.0 median ± IQR: 279.4 ± 1.4
ASTER	AST_08_00309262018212643_20231103031406_21563.SurfaceKineticTemperature	2018.09.26 21:26:43	mean ± SD: 281.9 ± 1.4 median ± IQR: 282.0 ± 1.7

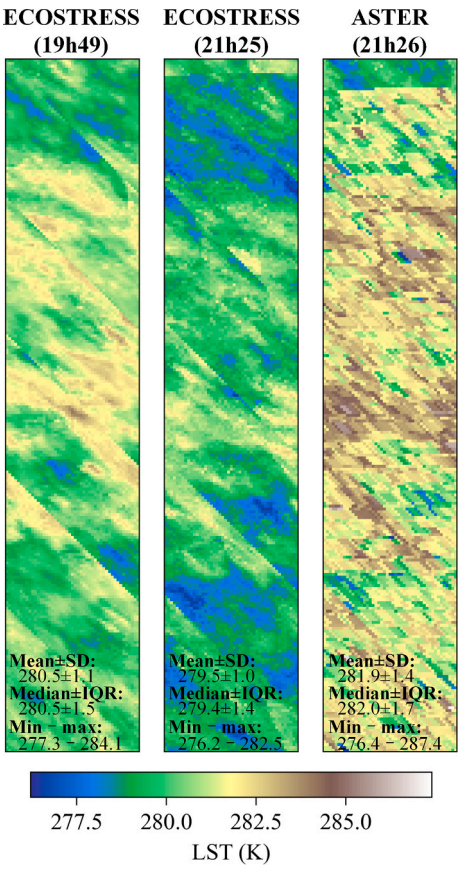

Fig. A.1. Land surface temperature (LST) images of ASTER and ECOSTRESS in the western areas of Brussels. SD: standard deviation. IQR: interquartile range.

ECOSTRESS LST products have a reported Root Mean Square Error (RMSE) of approximately 2.0 K, while ASTER LST products show an RMSE of 1.98 K (Hu et al., 2022). These error margins mean that cross-platform comparisons can introduce uncertainty ranges of up to $\sqrt{(2.0^2 + 1.98^2)} \approx 2.8$ K, which is a variation that could easily mask or distort the subtle temperature changes researchers aim to detect. In our case, the ASTER temperatures exceed ECOSTRESS readings by 2.4 K, despite only a around one-minute interval, which is a period typically characterized by minimal temperature fluctuations. This disparity, while falling within the combined error margins of both sensors, clearly demonstrates how cross-platform analyses can produce misleading results, and should be given adequate attention.

Data availability

The source code of TRUST-DART is distributed with the DART model, which is available on the DART website (https://dart.omp.eu/#/getDart). The source code of GeFolki is available on the website (https://github.com/aplyer/gefolki). The ASTER products are available at NASA (https://asterweb.jpl.nasa.gov/data_products.asp). The ECOSTRESS products are available at NASA (https://ecostress.jpl.nasa.gov/data). The Brussels mock-up is available at Urbis (https://datastore.brussels/web/urbis-download).

References

Abrams, M., Hook, S., Ramachandran, B., 2002. ASTER User Handbook, Version 2, 4800. Jet Propulsion Laboratory, p. 135.
Barducci, A., Pippi, I., 1996. Temperature and emissivity retrieval from remotely sensed images using the "grey body emissivity" method. IEEE Trans. Geosci. Remote Sens. 34, 681–695.
Bian, Z., Xiao, Q., Cao, B., Du, Y., Li, H., Wang, H., Liu, Q., Liu, Q., 2016. Retrieval of leaf, sunlit soil, and shaded soil component temperatures using airborne thermal infrared multiangle observations. IEEE Trans. Geosci. Remote Sens. 54, 4660–4671.
Bian, Z., Li, H., Göttsche, F.M., Li, R., Du, Y., Ren, H., Cao, B., Xiao, Q., Liu, Q., 2020. Retrieving soil and vegetation temperatures from dual-angle and multipixel satellite observations. IEEE J. Sel. Top. Appl. Earth Obs. Remote Sens. 13, 5536–5549.

Bian, Z., Fan, T., Roujean, J.-L., Wang, D., Irvine, M., Wu, S., Cao, B., Li, H., Du, Y., Xiao, Q., 2024. An analytical urban temperature model with building heterogeneity using geometric optical theory. Remote Sens. Environ. 301, 113948.
Bioucas-Dias, J.M., Plaza, A., Dobigeon, N., Parente, M., Du, Q., Gader, P., Chanussot, J., 2012. Hyperspectral unmixing overview: geometrical, statistical, and sparse regression-based approaches. IEEE J. Sel. Top. Appl. Earth Obs. Remote Sens. 5, 354–379.
Brigot, G., Colin-Koeniguer, E., Plyer, A., Janez, F., 2016. Adaptation and evaluation of an optical flow method applied to coregistration of forest remote sensing images. IEEE J. Sel. Top. Appl. Earth Obs. Remote Sens. 9, 2923–2939.
Cao, B., Liu, Q., Du, Y., Roujean, J.-L., Gastellu-Etchegorry, J.-P., Trigo, I.F., Zhan, W., Yu, Y., Cheng, J., Jacob, F., 2019. A review of earth surface thermal radiation directionality observing and modeling: historical development, current status and perspectives. Remote Sens. Environ. 232, 111304.
Chen, J.M., Liu, J., 2020. Evolution of evapotranspiration models using thermal and shortwave remote sensing data. Remote Sens. Environ. 237, 111594.
Chen, Y., Yang, K., He, J., Qin, J., Shi, J., Du, J., He, Q., 2011. Improving land surface temperature modeling for dry land of China. J. Geophys. Res. Atmos. 116.
Chen, J., Zhang, Y., Cihlar, J., Chen, W., 2016. Regional differences of land extreme precipitation and temperature changes under climate change condition. Plateau Meteorol. 35, 955–968.
Chen, S., Ren, H., Ye, X., Dong, J., Zheng, Y., 2021. Geometry and adjacency effects in urban land surface temperature retrieval from high-spatial-resolution thermal infrared images. Remote Sens. Environ. 262, 112518.
Chrysoulakis, N., Grimmond, S., Feigenwinter, C., Lindberg, F., Gastellu-Etchegorry, J.-P., Marconcini, M., Mitraka, Z., Stagakis, S., Crawford, B., Olofson, F., 2018. Urban energy exchanges monitoring from space. Sci. Rep. 8, 11498.
Cubero-Castan, M., Chanussot, J., Achard, V., Briottet, X., Shimoni, M., 2014. A physics-based unmixing method to estimate subpixel temperatures on mixed pixels. IEEE Trans. Geosci. Remote Sens. 53, 1894–1906.
Ding, L., Zhou, J., Li, Z.-L., Zhu, X., Ma, J., Wang, Z., Wang, W., Tang, W., 2023. Near-real-time estimation of hourly all-weather land surface temperature by fusing reanalysis data and geostationary satellite thermal infrared data. IEEE Trans. Geosci. Remote Sens. 61, 1–18.
Disney, M., Lewis, P., Gomez-Dans, J., Roy, D., Wooster, M., Lajas, D., 2011. 3D radiative transfer modelling of fire impacts on a two-layer savanna system. Remote Sens. Environ. 115, 1866–1881.
Duthoit, S., Demarez, V., Gastellu-Etchegorry, J.-P., Martin, E., Roujean, J.-L., 2008. Assessing the effects of the clumping phenomenon on BRDF of a maize crop based on 3D numerical scenes using DART model. Agric. For. Meteorol. 148, 1341–1352.
Fontanilles, G., Briottet, X., 2011. A nonlinear unmixing method in the infrared domain. Appl. Opt. 50, 3666–3677.
Francois, C., Ottlé, C., Prevot, L., 1997. Analytical parameterization of canopy directional emissivity and directional radiance in the thermal infrared. Application on the retrieval of soil and foliage temperatures using two directional measurements. Int. J. Remote Sens. 18, 2587–2621.
Gastellu-Etchegorry, J.-P., 2008. 3D modeling of satellite spectral images, radiation budget and energy budget of urban landscapes. Meteorog. Atmos. Phys. 102, 187–207.
Gastellu-Etchegorry, J.-P., Yin, T., Lauret, N., Cajgfinger, T., Gregoire, T., Grau, E., Feret, J.-B., Lopes, M., Guilleux, J., Dedieu, G., 2015. Discrete anisotropic radiative transfer (DART 5) for modeling airborne and satellite spectroradiometer and LIDAR acquisitions of natural and urban landscapes. Remote Sens. 7, 1667–1701.
Gastellu-Etchegorry, J.-P., Yin, T., Lauret, N., Grau, E., Rubio, J., Cook, B.D., Morton, D. C., Sun, G., 2016. Simulation of satellite, airborne and terrestrial LiDAR with DART (I): waveform simulation with quasi-Monte Carlo ray tracing. Remote Sens. Environ. 184, 418–435.
Gastellu-Etchegorry, J.-P., Lauret, N., Yin, T., Landier, L., Kallel, A., Malenovský, Z., Al Bitar, A., Aval, J., Benhmida, S., Qi, J., 2017. DART: recent advances in remote sensing data modeling with atmosphere, polarization, and chlorophyll fluorescence. IEEE J. Sel. Top. Appl. Earth Obs. Remote Sens. 10, 2640–2649.
Gillespie, A., Rokugawa, S., Matsunaga, T., Cothern, J.S., Hook, S., Kahle, A.B., 1998. A temperature and emissivity separation algorithm for advanced spaceborne thermal emission and reflection radiometer (ASTER) images. IEEE Trans. Geosci. Remote Sens. 36, 1113–1126.
Gonsamo, A., Croft, H., Chen, J.M., Wu, C., Froelich, N., Staebler, R.M., 2015. Radiation contributed more than temperature to increased decadal autumn and annual carbon uptake of two eastern North America mature forests. Agric. For. Meteorol. 201, 8–16.
Granero-Belinchon, C., Michel, A., Achard, V., Briottet, X., 2020. Spectral unmixing for thermal infrared multi-spectral airborne imagery over urban environments: day and night synergy. Remote Sens. 12, 1871.
Gustafson, W.T., Gillespie, A.R., Yamada, G.J., 2006. Revisions to the ASTER temperature/emissivity separation algorithm. In: Int. Symp. Recent Adv. Quant. Remote Sens.: Torrent (Valencia) Spain.
Hook, S.J., 2011. In: Pasadena, C.A. (Ed.), HyspIRI Level-2 Thermal Infrared (TIR) Land Surface Temperature and Emissivity Algorithm Theoretical Basis Document. Jet Propulsion Laboratory, National Aeronautics and Space Administration.
Hu, T., Mallick, K., Hulley, G.C., Planells, L.P., Göttsche, F.M., Schlerf, M., Hitzelberger, P., Didry, Y., Szantoi, Z., Alonso, I., 2022. Continental-scale evaluation of three ECOSTRESS land surface temperature products over Europe and Africa: temperature-based validation and cross-satellite comparison. Remote Sens. Environ. 282, 113296.
Huang, F., Zhan, W., Wang, Z., Wang, K., Chen, J.M., Liu, Y., Lai, J., Ju, W., 2017. Positive or negative? Urbanization-induced variations in diurnal skin-surface temperature range detected using satellite data. J. Geophys. Res. Atmos. 122, 13,229–13,244.
Hyndman, R.J., Koehler, A.B., 2006. Another look at measures of forecast accuracy. Int. J. Forecast. 22, 679–688.
Jiang, Y., Tang, R., Li, Z.-L., 2022. A framework of correcting the angular effect of land surface temperature on evapotranspiration estimation in single-source energy balance models. Remote Sens. Environ. 283, 113306.
Jiang, Y., Meng, X., Tang, R., Li, Z.-L., Bian, Z., Liu, J., 2024. Separate retrievals of soil and vegetation temperatures using two methods. Int. J. Remote Sens. 45, 7634–7653.
Jiménez-Muñoz, J.C., Sobrino, J.A., 2003. A generalized single-channel method for retrieving land surface temperature from remote sensing data. J. Geophys. Res. Atmos. 108.
Kallel, A., Ottle, C., Le Hegarat-Mascle, S., Maignan, F., Courault, D., 2012. Surface temperature downscaling from multiresolution instruments based on Markov models. IEEE Trans. Geosci. Remote Sens. 51, 1588–1612.
Kustas, W.P., Norman, J.M., 1999. Evaluation of soil and vegetation heat flux predictions using a simple two-source model with radiometric temperatures for partial canopy cover. Agric. For. Meteorol. 94, 13–29.
Landier, L., 2018. 3D modeling of the radiative budget of urban landscapes via the inversion of satellites images into urban materials reflectance and temperature maps. In: Centre d'Etudes Spatiales de la Biosphère. University of Toulouse, Toulouse.
Landier, L., Gastellu-Etchegorry, J., Al Bitar, A., Chavanon, E., Lauret, N., Feigenwinter, C., Mitraka, Z., Chrysoulakis, N., 2018. Calibration of urban canopies albedo and 3D shortwave radiative budget using remote-sensing data and the DART model. Eur. J. Remote Sens. 51, 739–753.
Lauwaet, D., De Ridder, K., Saeed, S., Brisson, E., Chatterjee, F., Van Lipzig, N., Maiheu, B., Hooyberghs, H., 2016. Assessing the current and future urban heat island of Brussels. Urban Clim. 15, 1–15.
Li, X., Strahler, A.H., Friedl, M.A., 1999. A conceptual model for effective directional emissivity from nonisothermal surfaces. IEEE Trans. Geosci. Remote Sens. 37, 2508–2517.
Li, Z., Petitcolin, F., Zhang, R., 2000. A physically based algorithm for land surface emissivity retrieval from combined mid-infrared and thermal infrared data. Sci. China Technol. Sci. 43, 23–33.
Li, Z., MP, S, Zhang, R., Jia, L., Su, Z., 2001. On the separate retrieval of soil and vegetation temperatures from ATSR data. Sci. China Ser. D Earth Sci. 44, 97–111.
Li, Z., Tang, B., Wu, H., Ren, H., Yan, G., Wan, Z., Trigo, I.F., Sobrino, J.A., 2013. Satellite-derived land surface temperature: current status and perspectives. Remote Sens. Environ. 131, 14–37.
Liu, Q., Yan, C., Xiao, Q., Yan, G., Fang, L., 2012. Separating vegetation and soil temperature using airborne multiangular remote sensing image data. Int. J. Appl. Earth Obs. Geoinf. 17, 66–75.
Liu, Y., Wu, C., Peng, D., Xu, S., Gonsamo, A., Jassal, R.S., Arain, M.A., Lu, L., Fang, B., Chen, J.M., 2016. Improved modeling of land surface phenology using MODIS land surface reflectance and temperature at evergreen needleleaf forests of Central North America. Remote Sens. Environ. 176, 152–162.
Liu, X., Tang, B., Li, Z., Zhou, C., Wu, W., Rasmussen, M.O., 2020. An improved method for separating soil and vegetation component temperatures based on diurnal temperature cycle model and spatial correlation. Remote Sens. Environ. 248, 111979.
Liu, W., Shi, J., Liang, S., Zhou, S., Cheng, J., 2022. Simultaneous retrieval of land surface temperature and emissivity from the FengYun-4A advanced geosynchronous radiation imager. Int. J. Digit. Earth 15, 198–225.
Liu, X., Li, Z., Duan, S., Leng, P., Si, M., 2025. Retrieval of global surface soil and vegetation temperatures based on multisource data fusion. Remote Sens. Environ. 318, 114564.
Ma, X.L., Wan, Z., Moeller, C.C., Menzel, W.P., Gumley, L.E., 2002. Simultaneous retrieval of atmospheric profiles, land-surface temperature, and surface emissivity from moderate-resolution imaging spectroradiometer thermal infrared data: extension of a two-step physical algorithm. Appl. Opt. 41, 909–924.
Ma, X., Zheng, G., Chi, X., Yang, L., Geng, Q., Li, J., Qiao, Y., 2023. Mapping fine-scale building heights in urban agglomeration with spaceborne lidar. Remote Sens. Environ. 285, 113392.
McMillin, L.M., 1975. Estimation of sea surface temperatures from two infrared window measurements with different absorption. J. Geophys. Res. 80, 5113–5117.
Michel, A., Granero-Belinchon, C., Cassante, C., Boitard, P., Briottet, X., Adeline, K.R., Poutier, L., Sobrino, J.A., 2021. A new material-oriented TES for land surface temperature and SUHI retrieval in urban areas: case study over Madrid in the framework of the future TRISHNA mission. Remote Sens. 13, 5139.
Mitraka, Z., Chrysoulakis, N., Kamarianakis, Y., Partsinevelos, P., Tsouchlaraki, A., 2012. Improving the estimation of urban surface emissivity based on sub-pixel classification of high resolution satellite imagery. Remote Sens. Environ. 117, 125–134.
Norman, J.M., Becker, F., 1995. Terminology in thermal infrared remote sensing of natural surfaces. Agric. For. Meteorol. 77, 153–166.
Ottlé, C., Vidal-Madjar, D., 1992. Estimation of land surface temperature with NOAA9 data. Remote Sens. Environ. 40, 27–41.
Pivovarník, M., Khalsa, S.J.S., Jiménez-Muñoz, J.C., Zemek, F., 2016. Improved temperature and emissivity separation algorithm for multispectral and hyperspectral sensors. IEEE Trans. Geosci. Remote Sens. 55, 1944–1953.
Plyer, A., Colin-Koeniguer, E., Weissgerber, F., 2015. A new coregistration algorithm for recent applications on urban SAR images. IEEE Geosci. Remote Sens. Lett. 12, 2198–2202.
RAMI5, 2021. RAMI-Benchmark: ACT_HET50_SAV_PRE, 2021. https://rami-benchmark.jrc.ec.europa.eu/_www/phase/phase_exp.php?strTag=level3&strNext=filter_testcases&strPhase=RAMI5&strTagValue=ACT_HET50_SAV_PRE.

Roupioz, L., Rodler, A., Guernouti, S., Al Bitar, A., Poutier, L., Briottet, X., Nerry, F., Musy, M., 2023. Monitoring LST at canyon scale for urban micro-climate applications: in-situ, simulation and airborne data comparisons. In: Joint Urban Remote Sens. Event. IEEE, pp. 1–4.

Ru, C., Duan, S.-B., Jiang, X.-G., Li, Z.-L., Huang, C., Liu, M., 2023. An extended SW-TES algorithm for land surface temperature and emissivity retrieval from ECOSTRESS thermal infrared data over urban areas. Remote Sens. Environ. 290, 113544.

Sánchez, J., Kustas, W., Caselles, V., Anderson, M., 2008. Modelling surface energy fluxes over maize using a two-source patch model and radiometric soil and canopy temperature observations. Remote Sens. Environ. 112, 1130–1143.

Sobrino, J., Romaguera, M., 2004. Land surface temperature retrieval from MSG1-SEVIRI data. Remote Sens. Environ. 92, 247–254.

Song, L., Liu, S., Kustas, W.P., Zhou, J., Ma, Y., 2015. Using the surface temperature-albedo space to separate regional soil and vegetation temperatures from ASTER data. Remote Sens. 7, 5828–5848.

Song, L., Bian, Z., Kustas, W.P., Liu, S., Xiao, Q., Nieto, H., Xu, Z., Yang, Y., Xu, T., Han, X., 2020. Estimation of surface heat fluxes using multi-angular observations of radiative surface temperature. Remote Sens. Environ. 239, 111674.

Su, Y., Zhang, C., Ciais, P., Zeng, Z., Cescatti, A., Shang, J., Chen, J.M., Liu, J., Wang, Y.-P., Yuan, W., 2023. Asymmetric influence of forest cover gain and loss on land surface temperature. Nat. Clim. Chang. 13, 823–831.

Thomas, L.L., William, R.J., 2015. ECOSTRESS Level 1 Focal Plane Array and Radiometric Calibration Algorithm Theoretical Basis Document (ATBD), 2015. https://lpdaac.usgs.gov/documents/222/Ecol1B_Calibration_ATBD_V1.pdf.

Tonooka, H., 2005. Accurate atmospheric correction of ASTER thermal infrared imagery using the WVS method. IEEE Trans. Geosci. Remote Sens. 43, 2778–2792.

Van Wilgen, B., Govender, N., Biggs, H., Ntsala, D., Funda, X., 2004. Response of savanna fire regimes to changing fire-management policies in a large African national park. Conserv. Biol. 18, 1533–1540.

Wan, Z., Li, Z., 1997. A physics-based algorithm for retrieving land-surface emissivity and temperature from EOS/MODIS data. IEEE Trans. Geosci. Remote Sens. 35, 980–996.

Wang, H., Mao, K., Shi, J., Bateni, S.M., Altantuya, D., Sainbuyan, B., Bao, Y., 2024a. A normal form for synchronous land surface temperature and emissivity retrieval using deep learning coupled physical and statistical methods. Int. J. Appl. Earth Obs. Geoinf. 127, 103704.

Wang, Y., Kallel, A., Zhen, Z., Lauret, N., Guilleux, J., Chavanon, E., Gastellu-Etchegorry, J.-P., 2024b. 3D Monte Carlo differentiable radiative transfer with DART. Remote Sens. Environ. 308, 114201.

Watson, K., 1992. Two-temperature method for measuring emissivity. Remote Sens. Environ. 42, 117–121.

Wicki, A., Parlow, E., Feigenwinter, C., 2018. Evaluation and modeling of urban heat island intensity in Basel, Switzerland. Climate 6, 55.

Xie, F., Shao, H., Liu, Z., Liu, C., Zhang, C., Yang, G., Wang, J., Cai, N., 2016. Retrieval of the pixel component temperatures from multi-band thermal infrared image using Bayesian inversion technique. In: Multispectral, Hyperspectral, and Ultraspectral Remote Sensing Technology, Techniques and Applications VI. International Society for Optics and Photonics, p. 98802A.

Zhan, W., Chen, Y., Zhou, J., Li, J., 2010. An algorithm for separating soil and vegetation temperatures with sensors featuring a single thermal channel. IEEE Trans. Geosci. Remote Sens. 49, 1796–1809.

Zhan, W., Chen, Y., Zhou, J., Wang, J., Liu, W., Voogt, J., Zhu, X., Quan, J., Li, J., 2013. Disaggregation of remotely sensed land surface temperature: literature survey, taxonomy, issues, and caveats. Remote Sens. Environ. 131, 119–139.

Zhao, W., Li, A., Bian, J., Jin, H., Zhang, Z., 2014. A synergetic algorithm for mid-morning land surface soil and vegetation temperatures estimation using MSG-SEVIRI products and TERRA-MODIS products. Remote Sens. 6, 2213–2238.

Zhen, Z., Gastellu-Etchegorry, J.-P., Chen, S., Yin, T., Chavanon, E., Lauret, N., Guilleux, J., 2021. Quantitative analysis of DART calibration accuracy for retrieving spectral signatures over urban area. IEEE J. Sel. Top. Appl. Earth Obs. Remote Sens. 14, 10057–10068.

Zhen, Z., Chen, S., Yin, T., Gastellu-Etchegorry, J.-P., 2022. Spatial resolution requirements for the application of temperature and emissivity separation (TES) algorithm over urban areas. IEEE J. Sel. Top. Appl. Earth Obs. Remote Sens. 15, 8990–9003.

Zhen, Z., Chen, S., Lauret, N., Kallel, A., Chavanon, E., Yin, T., León-Tavares, J., Cao, B., Guilleux, J., Gastellu-Etchegorry, J.-P., 2025. A gradient-based 3D nonlinear spectral model for providing components optical properties of mixed pixels in shortwave urban images. Remote Sens. Environ. 321, 114657.

Zheng, X., Li, Z., Nerry, F., Zhang, X., 2019. A new thermal infrared channel configuration for accurate land surface temperature retrieval from satellite data. Remote Sens. Environ. 231, 111216.

Zhou, S., Cheng, J., 2020. An improved temperature and emissivity separation algorithm for the advanced Himawari imager. IEEE Trans. Geosci. Remote Sens. 58, 7105–7124.

Zhou, X., Yang, K., Jiang, Y., Sun, J., Chen, Y., Li, X., Li, J., Shi, J., 2022. The influence of bare ground thermal roughness length parameterization on the simulation of near-surface air and skin temperatures over the Tibetan plateau. J. Geophys. Res. Atmos. 127, e2022JD037245.